Published in final edited form as:

Nature. 2022 June ; 606(7914): 594–602. doi:10.1038/s41586-022-04753-7.

ADAR1 masks the cancer immunotherapeutic potential of ZBP1-driven necroptosis

Ting Zhang[1,11], **Chaoran Yin**[1,11], **Aleksandr Fedorov**[2,11], **Liangjun Qiao**[3], **Hongliang Bao**[4], **Nazar Beknazarov**[2], **Shiyu Wang**[4], **Avishekh Gautam**[1], **Riley M. Williams**[1], **Jeremy Chase Crawford**[5], **Suraj Peri**[1], **Vasily Studitsky**[6,7], **Amer A. Beg**[8], **Paul G. Thomas**[5], **Carl Walkley**[9], **Yan Xu**[4], **Maria Poptsova**[2], **Alan Herbert**[2,10,*], **Siddharth Balachandran**[1,12,*]

[1]Blood Cell Development and Function Program, Fox Chase Cancer Center, Philadelphia, PA, USA.

[2]Laboratory of Bioinformatics, Faculty of Computer Science, National Research University Higher School of Economics, 11 Pokrovsky Bulvar, Moscow, Russia 101000

[3]College of Basic Medicine, Chongqing Medical University, Chongqing 400016, China

[4]Division of Chemistry, Department of Medical Sciences, Faculty of Medicine, University of Miyazaki, 5200 Kihara, Kiyotake, Miyazaki 889-1692, Japan.

[5]Department of Immunology, St. Jude Children's Research Hospital, Memphis, TN, USA.

[6]Cancer Signaling and Epigenetics Program, Fox Chase Cancer Center, Philadelphia, PA, USA.

[7]Biology Faculty, Lomonosov Moscow State University, Moscow 119992, Russia

[8]Department of Immunology and Thoracic Oncology, Moffitt Cancer Center and Research Institute, Tampa, Florida, USA.

[9]Cancer & RNA Biology, St. Vincent's Institute for Medical Research and Department of Medicine, St. Vincent's Hospital, University of Melbourne, Fitzroy 3065, VIC, Australia.

[10]InsideOutBio, 42 8th Street, Charlestown, MA

[11]Equal contribution

[12]Lead Contact

[*]Corresponding authors: S.B. Room 224 Reimann Building, 333 Cottman Ave., Philadelphia 19111. Phone: 215-214-1527; Fax: 215-728-3574; Siddharth.balachandran@fccc.edu. A.H. InsideOutBio, 42 8th Street, Charlestown, MA 02129, Phone: 617-584-0360; alan.herbert@insideoutbio.com.

Author contributions.

T.Z. and C.Y. carried out most of the cell culture and *in vivo* experiments, with assistance from A.G. and R.W. A.F. carried out most of the bioinformatics analyses, with assistance from N.B., L.Q., J.C.C, S.P, P.G.T., and C.W. H.B., S.W., and Y.X. carried out CD and NMR studies. C.W. provided lentiviral constructs for stable expression of ADAR1 p150 and its mutants. C.W. also provided immortalized $Adar^{-/-}$ MEFs, primary $Adar^{-/-}Ifih^{-/-}$ MEFs, and their controls. A.A.B. provided B16-OVA cells. A.A.B and P.G.T. assisted with immune cell analyses in tumor-bearing mice. M.P., V.S., A.H., and S.B. designed experiments, supervised the study, and analyzed the data. T.Z., C.Y., A.H. and S.B. wrote the manuscript. All authors participated in editing the manuscript.

Code availability

Detailed commands and scripts to reproduce the analysis are available online at GitHub: https://github.com/alnfedorov/MEF-CBL0137. The data preprocessing pipeline for the DeepZ model can be found at: https://github.com/Nazar1997/DeepZ_data_creation.

Declaration of Interests.

The authors declare no competing interests.

Abstract

A disappointingly small proportion of patients with cancer show lasting responses to immune checkpoint blockade (ICB)-based monotherapies. The RNA-editing enzyme ADAR1 is an emerging determinant of resistance to ICB therapy, and prevents ICB responsiveness by repressing immunogenic double-stranded (ds)RNAs, such as those arising from the dysregulated expression of endogenous retroviral elements (EREs)[1-4]. These dsRNAs trigger an interferon (IFN)-dependent antitumor response by activating A-form dsRNA (A-RNA)-sensing proteins such as MDA-5 and PKR[5]. Here, we show that ADAR1 also prevents accrual of endogenous Z-form dsRNA elements (Z-RNAs), which were enriched in the 3'UTRs of IFN-stimulated mRNAs. Depleting or mutating ADAR1 resulted in Z-RNA accumulation and activation of the Z-RNA sensor ZBP1, culminating in RIPK3-mediated necroptosis. As no clinically viable ADAR1 inhibitors currently exist, we searched for a compound that can override the requirement for ADAR1 inhibition and directly activate ZBP1. We identified a small molecule, the curaxin CBL0137, which potently activates ZBP1 by triggering Z-DNA formation in cells. CBL0137 induced ZBP1-dependent necroptosis in cancer-associated fibroblasts and strongly reversed ICB unresponsiveness in mouse models of melanoma. Collectively, these results demonstrate that ADAR1 represses endogenous Z-RNAs and identifies ZBP1-mediated necroptosis as a new determinant of tumor immunogenicity masked by ADAR1. Therapeutic activation of ZBP1-induced necroptosis provides a readily translatable avenue for rekindling immune responsiveness of ICB-resistant human cancers.

Reawakening endogenous retroviral elements (EREs) has emerged as a powerful means of stimulating innate immune signaling and kindling ICB responsiveness in cold tumors[5,6]. Adenosine Deaminase RNA Specific 1 (ADAR1) is a major repressor of immune responses activated by EREs[5,7-10]. ADAR1 binds ERE-derived dsRNAs and reduces their capacity to activate host dsRNA sensors, in part by introducing adenosine to inosine (A→I) edits in their sequences[9]. DsRNAs typically adopt the right-handed (A-RNA) conformation and are recognized by the dsRNA binding domains (dsRBDs) of ADAR1, preventing amplification of immune responses by host A-RNA sensors such as Melanoma Differentiation Antigen-5 (MDA-5) and Protein Kinase dsRNA-Dependent (PKR)[1-5,11-13] (Fig. 1a). When ADAR1 expression is ablated in tumors, these A-RNA sensors are activated, resulting in type I IFN cytokine production, loss of tumor cell fitness, and remarkably enhanced ICB responsiveness[1-5].

In addition to engaging A-form dsRNA, the interferon (IFN)-inducible p150 (but not p110) isoform of ADAR1 possesses a Zα domain, and can bind both left-handed Z-RNA and Z-DNA[14,15]. Intriguingly, Z-form nucleic acid Binding Protein 1 (ZBP1) has a related Zα domain that also binds Z-RNA and Z-DNA and is also induced by IFN. ZBP1 senses Z-RNAs and induces a hyperinflammatory form of nucleus-initiated necroptosis during influenza A virus infections[16]. These observations raise the possibility that ADAR1 p150 represses the accumulation of endogenous Z-RNAs which, if not squelched by ADAR1 p150, would serve as necroptosis-activating ligands for ZBP1 (Fig. 1a).

ADAR1 loss triggers Z-RNA accumulation.

To test if ADAR1 represses production of endogenous Z-RNAs, we ablated expression of *Adar*, the gene encoding ADAR1, by CRISPR approaches in immortalized wild-type (WT) murine embryo fibroblasts (MEFs) (Fig. 1b). We next cultured control *Adar* WT (ADAR1 WT) and *Adar*-deficient (ADAR1 KO) MEFs over a 10 day period, periodically fixing the cells in formaldehyde and examining them for the presence of Z-RNA using an antibody (clone Z22) originally raised to Z-DNA, but found by us and others to also detect Z-RNA *in vitro*[17] and *in cellulo*[16]. Cells lacking ADAR1 manifested a predominantly nuclear signal when stained with the Z22 antibody, detectable by day 4 post *Adar*-ablation, gradually increasing in intensity over 10 days. (Fig. 1c, d, Extended Data Fig. 1a, b). The signal produced by the Z22 antibody in ADAR1 KO MEFs was sensitive to RNase A but not to DNase I, strongly suggesting that it originated from the accumulation of endogenous Z-RNAs (Fig. 1e, f). Notably, ADAR1 KO MEFs also showed robust accumulation of A-RNA, with kinetics of induction largely paralleling that of Z-RNA (Fig. 1c-f, Extended Data Fig. 1a, b). Together, these results indicate that ADAR1, besides quenching cellular A-RNA, prevents the accumulation of endogenous Z-RNA.

Exposure of ADAR1 KO MEFs to anti-IFNAR1 neutralizing antibodies, or following *Mavs* ablation, prevented accumulation of Z-RNAs (and A-RNAs), indicating that RIG-I-like receptor - driven type I IFN signaling was largely responsible for the accrual of dsRNAs in the absence of ADAR1 (Extended Data Fig. 1a-c). Exposing ADAR1 KO MEFs to exogenous (recombinant) IFNβ strongly stimulated production of both Z-RNA and A-RNA within 48 hrs (Fig. 1g, h). IFNβ signaling is not significantly affected by ADAR1 deficiency (Extended Data Fig. 1d, e), and IFN-driven Z-RNA accrual was also seen in primary MEFs from *Adar*-deficient mice, as well as in immortalized murine macrophages, epithelial cells, and endothelial cells in which *Adar* was ablated by CRISPR-based approaches (Extended Data Fig. 1f-m). By reconstituting immortalized $Adar^{-/-}$ MEFs with mutants of ADAR1 p150 that are incapable of either binding Z-RNA (N175A/Y179A)[18] or editing dsRNA substrates (E861A)[13], we found that ADAR1 repressed endogenous Z-RNAs in a manner that required a functional Zα domain, but was only partially dependent on its editing activity (Fig. 1i, , Extended Data Fig. 1n-p). The enzyme-null ADAR1 mutant likely represses IFN-stimulated Z-RNAs by direct sequestration, because proteinase K-mediated elimination of ADAR1 E861A protein post fixation restored the Z-RNA signal in these cells to levels seen in $Adar^{-/-}$ MEFs carrying an empty vector control (Extended Data Fig. 1q-t).

To identify endogenous Z-RNAs repressed by ADAR1, we ablated ADAR1 expression in $Zbp1^{-/-}$ MEFs, and used the Z22 antibody to immuno-precipitate Z-RNAs from these cells following IFNβ treatment. Ablating *Adar* in $Zbp1^{-/-}$ MEFs not only eliminates any potential competition from ZBP1 or ADAR1 for Z-RNAs pulled down by the Z22 antibody, but also prevents ZBP1-dependent cell death triggered by these Z-RNAs. Sequencing Z22-enriched RNAs demonstrated that most (> 90%) of the RNAs were protein-coding mRNAs; intergenic, ncRNA, and other non-mRNA species comprised the rest of the reads (Extended Data Fig. 2a). A substantial fraction (21.3 %) of the Z22 enriched RNAs were ISG mRNAs, representing a far larger proportion of the enriched pool of mRNAs than their prevalence in the overall transcriptome (hypergeometric mean *p*-value: 2.73×10^{-24}). A

total of 355 ISG mRNAs were enriched in Z22 pulldowns from ADAR1 KO *Zbp1*$^{-/-}$ MEFs (Fig. 1k, Supplementary Table. 1). Given that type I IFN signaling generates the Z-RNA signal unmasked by ADAR1 p150 loss (Fig. 1g, Extended Data Fig. 1a-c), we focused our subsequent analyses on these Z22-enriched ISGs.

To identify ADAR1 editing targets amongst the Z-RNA-forming ISG mRNAs, we sequenced Z22-bound mRNAs from ADAR1 WT MEFs and assessed the degree of A→I editing in these mRNA sequences by calculating their editing index[19], a robust, normalized, and quantitative measure of global A→1 modification. In the absence of IFNβ treatment, Z22-associated mRNAs displayed an editing index of ~0.1% (Extended Data Fig. 2b), occurring more frequently than other transitions or transversions (which were found at ~0.06% in our dataset, inclusive of sequencing errors). The low basal level of editing likely results from ADAR2 activity as ADAR1 p150 levels are typically very low in unstimulated MEFs (e.g., Fig. 1b), with ADAR2 protein levels and ISG RNA editing indices equivalent between resting ADAR1 WT and KO cells (Extended Data Fig. 2b, c). RNAs in Z22 pulldowns from IFNβ-exposed ADAR1 WT MEFs displayed a significantly increased editing index compared to either untreated ADAR1 WT cells (~6-fold) or IFNβ-treated ADAR1 KO MEFs (~10-fold) (Extended Data Fig. 2b). This increase in the editing index is therefore attributable to IFN-induced expression of the ADAR1 p150 isoform[12], its binding of Z-RNA through the Zα domain, and the subsequent editing of these Z-RNAs.

We next compared Z22 enriched ISG mRNAs isolated from ADAR1 KO *Zbp1*$^{-/-}$ MEFs to those displaying evidence of A→I editing in Z22 pulldowns from IFNβ-treated ADAR1 WT MEFs. Among the 355 ISG mRNAs enriched by the Z22 antibody, only 14 were strongly edited by ADAR1 in IFN-stimulated WT cells (editing index > 0.5%). Of the 26 hyper-edited loci observed in these 14 ISG mRNAs, 21 (~84%) were in SINE-containing 3'UTRs (Extended Data Fig. 2d, Supplementary Table. 1). Examining these SINE-containing sequences revealed that most (15/21) of the A→I edits occurred within dsRNA formed by the base-pairing of inverted SINE repeats (i.e., two adjacent SINEs in opposite orientation to each other) (Extended Data Fig. 2d, Supplementary Table. 1). Overall 393 SINEs were cumulatively seen in our dataset (found in 163 of the 355 Z22-enriched ISG mRNAs), but only the small subset of Z-forming mRNAs with inverted SINEs in their 3'UTRs were preferred ADAR1 p150 editing targets. We selected for further analysis three ISG mRNAs with high editing indices and inverted SINEs in their 3'UTRs (*Slfn5, Xrn1, Knl1*). Each of these 3'UTRs were also robustly pulled down in an IFN-dependent manner by Z22, but not by a control IgG, from ADAR1 KO lysates (Fig. 1l, Extended Data Fig. 2e). Therefore, ISG 3'UTRs containing dsRNA-forming inverted SINEs are one class of ADAR1-repressed endogenous Z-RNAs.

Interestingly, a significant subset of Z22-enriched ISG mRNAs (156/355) contained at least one Z-prone simple repeat (Extended Data Fig. 2d; Supplementary Table. 1). As with inverted SINEs, the 42 GU-type simple repeats (i.e., GU-rich stretches of 6 or more bases)[20] were present solely in the 3'UTRs of Z22 bound ISG mRNAs. Only one GU-type simple repeat showed evidence of editing, suggesting that ADAR1 p150 sequestration of this simple repeat class of Z-RNAs is sufficient to prevent ZBP1 activation. Indeed, catalytic-dead ADAR1 p150 still suppresses Z-RNA accrual (Fig. 1i, j), indicating that sequestration is an

important means by which ADAR1 p150 squelches endogenous Z-RNAs. The ISG mRNAs encoding the dsRNA sensors PKR (*Eif2ak2*), RIG-I (*Ddx58*), and MDA-5 (*Ifih1*) all lacked inverted SINEs, but harbored GU-type simple repeats (Fig. 1m, Extended Data Fig. 2f). We confirmed by RT-qPCR that each of these 3'UTRs were also specifically pulled down by the Z22 antibody in the absence of ADAR1, and that IFN treatment increased the abundance of these RNAs in Z22 pulldowns (Fig. 1m, Extended Data Fig. 2f). Examining the GU-rich sequences of these simple-repeat containing 3'UTRs indicate that they are potentially capable of folding into the shape of a dumbbell, with multiple putative core Zα binding sites of 4 base pairs within a longer dsRNA duplex (Fig. 1m, Extended Data Fig. 2f, pink boxes). To test if such dumbbell sequences were prone to forming Z-RNA, we synthesized a consensus dumbbell comprising the potential Z-forming and Zα binding core features observed in the Z22-enriched 3'UTR sequences (Fig. 1n), and examined its capacity to form Z-RNA *in vitro*. We found that the dumbbell, but not a control RNA, was capable of forming Z-RNA *in vitro*, although, as with unmodified Z-forming sequences[21], high salt concentrations were required for stable Z-RNA formation (Fig. 1n). Additional constraints in the 3'UTRs of the endogenous RNAs, such as base modification or protein binding, may therefore stabilize these dumbbell structures in the Z-conformation in cells. Altogether, these results demonstrate that both SINE-containing sequences, as well as GU-type simple repeat 'fold-back' sequences within the 3'UTRs of ISG mRNAs, form Z-RNAs in cells and are repressed by ADAR1. Besides SINEs and simple repeats, we observed LTRs, LINEs, and low-complexity repeats in several Z22-enriched ISG mRNAs (Extended Data Fig. 2d); although none of these were significant ADAR1 editing targets, they may also represent Z-RNA forming ligands for ZBP1.

ADAR1 loss activates ZBP1-driven necroptosis.

We noticed that WT MEFs (i.e., expressing ZBP1) in which ADAR1 was acutely ablated by CRISPR approaches began dying by 7 days post ADAR1 loss, about 3 days after Z-RNA accumulation was first observed (Extended Data Fig. 1a), suggesting that ADAR1 loss induces Z-RNA-triggered ZBP1-dependent cell death. To explore this possibility, we generated immortalized *Zbp1*$^{-/-}$ MEFs stably expressing either FLAG-tagged wild-type murine ZBP1 or an empty vector control, ablated *Adar* in these cells, and observed them over a 12-day period. ADAR1 loss in FLAG-ZBP1-reconstituted MEFs resulted in arrested proliferation by day 6, followed by progressive IFN-dependent loss of viability between days 7 and 12. In contrast, *Zbp1*$^{-/-}$ MEFs carrying an empty vector underwent proliferation arrest by day 7, yet remained viable for the duration of the study (Fig. 2a). Exposing ADAR1 KO (but ZBP1 wild type) cells to recombinant IFNβ triggered ZBP1-dependent cell death within 48 hrs of treatment (Fig. 2b, Extended Data Fig. 3a). Of a panel of inflammatory cytokines tested, only IFNβ and IFNγ, but not IL-1α, TNFα, or TRAIL, induced ZBP1-dependent cell death in ADAR1-deficient MEFs (Extended Data Fig. 2b). IFN-activated cell death was rescued by the combination of the pan-caspase blocker zVAD and the RIPK3 kinase inhibitor GSK'843 (R3i), but not either agent alone, demonstrating that death was a combination of apoptosis and necroptosis (Extended Data Fig. 3c,d), as we have previously shown with IAV[16]. In agreement, ablating *Adar* in necroptosis-deficient *Mlkl*$^{-/-}$ MEFs sensitized these cells to IFNβ-induced cell death, but such death was solely

apoptosis (i.e., prevented by either zVAD or by co-deletion of caspase 8; Extended Data Fig. 3e). Of note, ADAR1 deficiency did not sensitize cells to necroptosis by altering the protein levels of RIPK1, FADD, or caspase 8 (Extended Data Fig. 3f).

Cells reconstituted with ZBP1 mutants incapable of either sensing Z-RNA (Zα2mut or ΔZα) or associating with RIPK3 (RHIM-Amut) did not succumb to IFNβ upon ADAR1 ablation, suggesting that ZBP1 sensed endogenous Z-RNAs unleashed by ADAR1 loss to activate RIPK3-dependent cell death (Extended Data Fig. 3g-i). We found that stimulating ADAR1 KO cells with IFNβ caused FLAG-ZBP1, but not a Zα deletion mutant (FLAG-ΔZα), to co-localize with nuclear Z-RNA (Fig. 2c, d). Examining ZBP1-associated RNAs from IFNβ-treated ADAR1 KO cells by RT-qPCR showed that FLAG-ZBP1, but not FLAG-ΔZα, bound the 3'UTRs of Z-RNA-forming ISG mRNAs (both those with inverted SINEs and with GU-type repeats) identified in Z22 pulldowns (Extended Data Fig. 3j-l). Thus, Z-RNA sequences within the 3'UTRs of ISG mRNAs are *bona fide* ligands for ZBP1 in ADAR1-deficient cells.

Following activation, ZBP1 complexed with RIPK3 and MLKL, and induced phosphorylation of MLKL in IFN-treated ADAR1 KO cells (Fig. 2e). Phosphorylated MLKL was observed first in the nucleus, after which it migrated to the cytosol and the plasma membrane (Extended Data Fig. 3m, n). Notably, MLKL activation was associated with detectable rupture of the nuclear envelope in ~30% of immortalized ADAR KO MEFs at 48 hrs post IFNβ treatment (Extended Data Fig. 3o, p). Altogether, these findings show that endogenous Z-RNAs associate with and activate ZBP1 in the nucleus when ADAR1 is absent. ZBP1-driven 'nuclear necroptosis' is thus a heretofore unappreciated arm of the innate immune response to endogenous dsRNA (Fig. 2f).

CBL0137 induces Z-DNA formation in mammalian genomic DNA.

No clinically viable small-molecule inhibitors specific for ADAR1 are currently available. Nor has direct activation of ZBP1 by synthetic Z-RNA been proven tractable[17,21]. Z-DNA, however, shares almost-identical structures with Z-RNA (Extended Data Fig. 4a), and ZBP1 binds both Z-DNA and Z-RNA *in vitro*[22,23]. Importantly, Z-DNA can be generated in eukaryotic cells from negative supercoiling or epigenetic modification of genomic DNA[10,24] Reasoning that agents capable of generating Z-DNA in cells will directly activate ZBP1, overriding the need either for ADAR1 inhibitors or synthetic Z-RNA, we carried out a curated screen for small-molecule inducers of Z-DNA formation, focusing on compounds known to intercalate DNA, affect DNA topology, or alter chromatin structure and dynamics. We treated cells with equimolar (5μM) amounts of each compound and assessed Z-DNA formation by immunofluorescence using the Z22 antibody, which recognizes both Z-RNA and Z-DNA[17]. We identified the second-generation curaxin family member CBL0137, as well as a number of its analogs, as potent inducers of Z-DNA in mammalian cells (Fig. 3a-c, Extended Data Fig. 4b, c). CBL0137 is best-characterized as an inhibitor of the histone chaperone FACT[25], but it also directly intercalates DNA[26]. The signal generated by the Z22 antibody in CBL0137-treated cells was sensitive to DNase I, but not RNase A or RNase H, indicating it originated predominantly from Z-DNA, rather than from Z-RNA or DNA:RNA hybrids (Fig. 3b, c). By immuno-precipitating and sequencing Z-DNA from

CBL0137-treated MEFs, we found that CBL0137 induced Z-DNA formation in hundreds of sites across the mouse genome, the majority of which mapped to long interspersed nuclear element (LINE)1 retroviral DNA (Fig. 3d). In particular, LINE1 elements encoding full-length L1Md A and L1Md T were highly enriched in Z22 pulldowns of CBL0137-treated cells (Fig. 3d, right; Extended Data Fig. 4d) compared to their frequency within the mouse genome (Fig. 3d, left). L1Md A- and L1Md T-forming Z-DNA sites in CBL0137-treated cells were primarily intergenic (~77% of L1Md A and ~70% of L1Md T), with a smaller proportion found within introns (~15% of L1Md A and ~20% of L1Md T) (Fig. 3e). L1Md A and L1Md T comprise less than 2.5% of the mouse genome, yet represent about half (~46%) of all full-length LINE1 elements[27]. In examining the sequences of these two LINE1 elements, we noticed that their 5'UTRs contained GC-rich sequences and are predicted by our DeepZ algorithm[28] to be predisposed to Z-DNA formation (Fig. 3f). As will be shown later (Fig. 4j), the Z22 binding peak was also within the 5'UTRs of these LINE1 elements, situated ~450 bp from their 5' termini, suggesting that CBL0137 may trigger Z-DNA formation by inducing the B→Z conversion of Z-prone B-DNA.

To directly test if CBL0137 could convert Z-prone B-DNA to Z-DNA *in vitro*, we synthesized a GC-rich B-DNA octamer incorporating, into one strand of the duplex, 2'-*O*-methyl-8-methyl modification of internal guanosine nucleosides (m^8Gm). The introduction of a methyl group at the C8 position strongly facilitates the B→Z transition[29]. In the absence of CBL0137, the m^8Gm dsDNA octamer was in the B-conformation when examined by circular dichroism, but it flipped into the Z-conformation with the addition of equimolar (1:1) amounts of CBL0137 (Fig. 3g). This effect was even more pronounced at a higher ratio (2:1) of CBL0137 to B-DNA. ^{19}F NMR demonstrated that CBL0137 diminished the Z-DNA peak during formation of the DNA/CBL0137 complex (Fig. 3h). Together, the *in vitro* results suggest that CBL0137 can promote the B→Z transition in dsDNA, when facilitated by base modifications aiding this transition. CBL0137 may additionally induce a B→Z transition in cells by displacing FACT or other proteins from histone linker regions, resulting in topological stress and Z-DNA formation by Z-prone sequences[25]. This possibility is supported by our finding that DNA sequences in Z22 pulldowns were also enriched in epigenetic marks and histone variants associated with FACT activity (e.g., H2A.Z)[30], and for sites interacting with the FACT subunit SSRP1 (Extended Data Fig. 4e-g, Supplementary Table. 2). CBL0137 also induced the loss of PML bodies normally associated with suppression of L1 transcription[31] (Extended Data Fig. 4h, i), suggesting that Z-DNA formation may also arise from transcription of L1 elements; these and other possibilities warrant further exploration.

CBL0137 potently triggers ZBP1-dependent necroptosis.

We found that CBL0137 at 5 μM induced robust ZBP1-dependent death in ~90% of immortalized MEFs by 24 hrs (Fig. 4a, b). Death was blocked by co-treatment with zVAD and the RIPK3 inhibitor GSK'843 (Fig. 4c). Co-deletion of *Mlkl* and *Casp8*, but not *Mlkl* alone, protected MEFs from CBL0137 (Extended Data Fig. 5a). Together, these results demonstrate that ZBP1 activates both apoptosis and necroptosis following CBL0137 exposure, similar to the what we have observed in other scenarios of ZBP1 activation, such as upon ADAR1 loss (Extended Data Fig. 3c, d) and during IAV infection[16]. CBL0137 also

induced Z-DNA formation and ZBP1-dependent cell death in primary MEFs (Extended Data Fig. 5b-e), as well as in the immortalized human fibroblast cell line HS68, in which ZBP1 expression is hIFNβ inducible (Extended Data Fig. 5f-j). ZBP1-induced cell death was accompanied by phosphorylation of MLKL (Fig. 4d; Extended Data Fig. 5e, j) and cleavage of procaspase-3 (Fig. 4d). Cell death and MLKL activation in MEFs required the Zα domains and RHIM of ZBP1 (Extended Data Fig. 5k, l). CBL0137 induced the translocation of ZBP1 into the nucleus (Fig. 4e) and its co-localization with Z-DNA in most treated MEFs (Fig. 4f). CBL0137 also induced ZBP1-independent caspase activity in MEFs (Fig. 4d), which manifested as apoptosis after 18-24 hrs, likely accounting for its previously reported oncocidal effects in tumor derived-cell lines, most of which are RIPK3-deficient[32-35]. In this regard, we found that CBL0137 triggered robust Z-DNA formation in primary bone-marrow derived macrophages (BMDMs; Extended Data Fig. 5m). Although CBL0137-induced death in BMDMs involves additional ZBP1-independent pathway(s) (Extended Data Fig. 5n), BMDMs are a source of myeloid-derived-suppressor cells (MDSCs) *in vivo*[36], and MDSC depletion by CBL0137 may contribute to the antitumor effects of this agent.

We next treated immortalized *Zbp1*$^{-/-}$ MEFs stably expressing FLAG-ZBP1 with CBL0137 for 14 hrs, immunoprecipitated FLAG-ZBP1 from these cells, and performed ChIP-seq on the eluted DNA. ZBP1-bound DNAs mapped to numerous sites across the entire mouse genome (Fig. 4g, blue peaks). A large fraction of fragments bound by ZBP1 after CBL0137 exposure overlapped with the sites independently detected by ChIP-seq using the Z-DNA specific Z22 antibody (Fig. 4g, magenta peaks; overlapping sites are depicted by purple bars). The majority (58%) of overlapping peaks bound by both Z22 and ZBP1 were full-length LINE1 elements (Fig. 4h, i). As with Z22 (Fig. 3d), most of these ZBP1-bound sequences mapped to the 5'UTRs of L1Md A and L1Md T elements (Fig. 4j, Extended Data Fig. 5o), confirming that these sequences were prone to forming Z-DNA. We validated by RT-qPCR that the 5'UTRs of L1Md A and L1Md T elements were bound, following CBL0137 treatment, by both the Z22 antibody and FLAG-ZBP1, but not an isotype control antibody (IgG) or FLAG-ΔZα (Fig. 4k, Extended Data Fig. 5p). Consequently, CBL0137 triggered an association between ZBP1, RIPK3 and MLKL (Fig. 4l), causing the activation of MLKL that was observed first in the nucleus (Fig. 4m), and then in the cytoplasm (Fig. 4n), leading to ZBP1-dependent rupture of the nuclear envelope (Fig. 4o), and resulting in nuclear necroptosis (Fig. 4p).

CBL0137 reverses ICB resistance by inducing ZBP1-initiated necroptosis in tumor fibroblasts.

CBL0137 induced Z-DNA formation in all human cell lines tested (Extended Data Fig. 6a, b), and robustly triggered death in human and murine cells competent for ZBP1/RIPK3-driven death signaling (Extended Data Fig. 6c-e), suggesting that this compound will be useful as a potential ZBP1 agonist in human cancers. To leverage our findings for cancer immunotherapy, we focused on malignant melanoma, a tumor type in which ICB has shown promise, but where therapy resistance is a significant problem[37]. Analysis of data from melanoma specimens in The Cancer Genome Atlas (TCGA) showed that tumors with intact necroptosis machinery manifested significantly greater levels of infiltrating monocytes and

CD8$^+$ T cells, indicating that activation of ZBP1-dependent necroptosis in tumors has the potential to trigger beneficial adaptive immune responses in melanoma (Fig. 5a). A majority (~60%) of tumors were either low in necroptosis gene expression, or did not express the necroptosis machinery to any detectable extent, paralleling what is seen in most human tumor-derived cell lines[35]. These tumors were also proportionately devoid of immune cells (Fig. 5a). Nonetheless, all melanomas showed significant fibroblastic infiltrate (Fig. 5a), and an analysis of scRNA-seq data[2] from the ICB-refractory murine melanoma (B16-F10) revealed that tumor infiltrating fibroblasts are likely necroptosis competent (Fig. 5b).

These observations led us to hypothesize that inducing necroptosis by triggering ZBP1 activation in TME stromal cells (such as cancer-associated fibroblasts) would induce potent antitumor responses and potentiate ICB therapy. Further, such an approach would be of great clinical significance as it does not require the cancer cells to be necroptosis-competent. To test this hypothesis, we generated B16-F10 melanoma syngeneic tumors in wild-type C57BL/6J mice, and injected CBL0137 into these tumors. We then assessed Z-DNA formation at 16 hrs and necroptosis activation at 24 hrs post injection. We found that CBL0137 induced rampant Z-DNA formation in cells surrounding the injection site, including in fibroblasts of the TME, as determined by co-staining tumor sections for Z-DNA and the fibroblast marker PDGFRα (Fig. 5c). Quantifying these results showed that CBL0137 induced Z-DNA formation in >60% of TME fibroblasts (Fig. 5d). Staining sections for pMLKL from CBL0137-treated B16-F10 tumors generated in wild-type or *Zbp1*$^{-/-}$ mice showed that CBL0137 activated necroptosis in a majority (~70%) of TME fibroblasts in wild-type mice, but not *Zbp1*$^{-/-}$ mice, demonstrating that necroptosis was dependent on host expression of ZBP1 (Fig. 5e, f).

To examine whether necroptosis induced by CBL0137 in TME fibroblasts was able to reverse ICB non-responsiveness in a mouse model, we produced B16-F10 tumors in either wild-type or *Zbp1*$^{-/-}$ recipients. We then treated these mice with four cycles of either CBL0137 or a vehicle control (intra-tumorally), in combination with either an anti-PD-1 antibody or an isotype control antibody (systemically, by intraperitoneal administration; Fig. 5g). We found that treatment with both CBL0137 and anti-PD-1 antibody, but not either agent alone, induced recruitment of CD3$^+$CD8$^+$ T cells into the tumor by day 11 post-initiation of treatment (Fig. 5h, i). These CD8$^+$ T cells displayed markers of activation (CD44), effector function (GzmB), and proliferation (Ki67), and were accompanied by a significant increase in the abundance of CD11c$^+$ dendritic cells (DCs; Extended Data Fig. 6f). T cell and DC influx into the tumor was only seen in wild-type animals, and not in *Zbp1*$^{-/-}$ mice (Fig. 5h, i, Extended Data Fig. 6f), demonstrating that ZBP1-dependent necroptosis was responsible for their recruitment. We next produced B16-OVA (i.e., B16 cells expressing chicken ovalbumin) tumors in mice, treated animals with CBL0137 or a vehicle control (intra-tumorally), in combination with either an anti-PD-1 antibody or an isotype control antibody (i.p.), and examined tumor draining (inguinal) lymph nodes (tdLNs) for the presence of OVA-specific (SIINFEKL H-2K^b) CD8$^+$ T cells. CBL0137 plus anti-PD-1 antibody treatment, but not either agent alone, induced a significant increase in the total number and frequency (as a proportion of all CD8$^+$ T cells) of OVA-specific CD8$^+$ T cells in tdLNs (Extended Data Fig. 6g-i). In agreement with these observations, anti-PD-1 antibody, when combined with CBL0137, was able to induce significant regression of

B16-F10 tumors only in wild-type mice, but not in *Zbp1*$^{-/-}$ mice (Fig. 5j). Moreover, intratumoral CBL0137 also potentiated an abscopal response to systemic anti-PD-1 antibody treatment in the B16-OVA tumor model (Extended Data Fig. 6j, k).

We further tested the effects of CBL0137 on anti-PD-1 antitumor responses on YUMMER1.7 tumors. This model is considered more clinically-relevant than the B16-F10 model, because YUMMER1.7 cells were obtained from a UV-induced murine melanoma, and because they are only partially responsive to anti-PD-1 monotherapy[38], mirroring clinical outcomes for human melanoma[37]. We found that anti-PD-1 antibody treatment by itself was able to induce the regression of a fraction of these tumors (Fig. 5k); however, CBL0137 triggered Z-DNA formation and activated ZBP1-dependent necroptosis in fibroblasts of the YUMMER1.7 TME (Extended Data Fig. 6l-o), and the combination of CBL0137 and anti-PD-1 antibody induced complete tumor regression in almost all treated wild type mice, but not in *Zbp1*$^{-/-}$ mice (Fig. 5k). Altogether, these results demonstrate that CBL0137, by inducing ZBP1-dependent necroptosis in cells of the TME, drives $CD8^+$ T cell recruitment into tumors and strongly potentiates ICB responses *in vivo.*

Discussion.

We demonstrate that ADAR1 p150 represses Z-RNA accrual and ZBP1-dependent necroptosis by preventing the accumulation of mRNA transcripts capable of forming Z-RNAs. Such Z-forming sequence, which we call 'flipons'[10], are enriched in the 3′ UTRs of ISG mRNAs harboring either inverted SINEs or GU-type simple repeats capable of folding into Z-prone dumbbells. To weaponize ZBP1-driven necroptosis as an adjuvant for cancer immunotherapy, we describe a small molecule which forces genomic sequences to adopt the Z-DNA conformation, bypassing ADAR1 dependent immune silencing within tumors and directly activating ZBP1 dependent 'nuclear necroptosis' in tumor stromal fibroblasts.

We have previously shown[16] that such nuclear necroptosis is significantly more immunogenic than cytoplasm-induced necroptosis as it results in the release from the nucleus of numerous DAMPs (such as HMGB-1, IL-33, and, indeed, DNA itself)[16]. CBL0137 was able to reverse ICB unresponsiveness in a refractory model of cutaneous malignant melanoma, as well as in a clinically relevant model of this malignancy. Importantly, CBL0137 manifested these effects by activating ZBP1 in fibroblasts of the TME, rather than within the tumor cells themselves, indicating that this agent will be agnostic to the driver mutations within tumors, and provide therapeutic benefit even when cancer cells are necroptosis-incompetent.

Notably, CBL0137 has been well-tolerated in human Phase 1 clinical trials, perhaps because of low/absent basal ZBP1 levels in many normal cell types. ZBP1 expression is, however, strongly induced by IFN. The chronic IFN signature characterizing many tumors[39,40] may upregulate ZBP1 expression selectively in cells of the TME, offering an unexpected therapeutic window for both intralesional and systemic administration of CBL0137 in clinical settings. Of relevance here, CBL0137 administered intravenously at a dose achievable therapeutically also induces Z-DNA formation in tumors (Extended Data Fig. 6p, q). As the genes encoding MLKL, MDA-5, and PKR are also IFN inducible, elevated tonic

IFN signaling in the TME may in fact represent a potential tumor vulnerability exploitable not only by CBL0137, but also by ADAR1 inhibitors (which will increase both A- and Z-form dsRNA-initiated immunogenic responses), and by ZBP1-activating viruses, such as the HSV-1-based oncolytic agent talimogene laherparepvec (T-vec).

Methods.

Mice

Zbp1$^{-/-}$ mice have been described previously[1] and were backcrossed onto the C57BL/6 background for 12 generations before use alongside littermate matched *Zbp1*$^{+/+}$ mice in tumor studies. In some experiments (e.g., those not requiring *Zbp1*$^{-/-}$ animals), C57BL/6J mice were obtained from the Jackson Laboratory and were allowed at least one week to acclimate to housing conditions at the Fox Chase Cancer Center before use in experiments. Eight-to-ten week old female mice were used in all studies. All experimental mice were housed under specific pathogen-free conditions and all *in vivo* experiments were conducted under protocols approved by the Committee on Use and Care of Animals at the Fox Chase Cancer Center and St. Vincent's Hospital. No statistical methods were used to predetermine sample size. The experiments were not randomized. The investigators were not blinded to allocation during experiments.

Cell lines

WT, *Zbp1*$^{-/-}$, *Mlkl*$^{-/-}$, and *Mlkl*$^{-/-}$*Casp8*$^{-/-}$ MEFs were generated from E14.5 embryos, and immortalized using a 3T3 protocol. *Adar*$^{-/-}$ and *Adar*$^{-/-}$*Ifih1*$^{-/-}$ MEFs were isolated from E11.5 or E14.5 embryos respectively[2]. *Adar*$^{-/-}$ MEFs were immortalized using an shRNA against p53 (pLMP-p53.1224; gift from Ross Dickins, Monash University). Primary and immortalized MEFs were maintained in DMEM supplemented with 15% FBS, 1 mM sodium pyruvate, 1 × GlutaMAX, and 1% penicillin/streptomycin. Immortalized *Zbp1*$^{-/-}$ and *Adar*$^{-/-}$ MEFs were stably reconstituted with expression constructs using the Retro-X retroviral or pLVX-Puro lentiviral transduction systems. Immortalized BMDMs, LET1, SVEC4-10, HS68, Hep G2, MCF-7, HT-29, HeLa and A375 cells were maintained in DMEM supplemented with 10% FBS, 1 × GlutaMAX, and 1% penicillin/streptomycin. B16-F10 (ATCC, CRL-6475), A549, SK-MEL-2 and B16-OVA cells were cultured in RPMI-1640 supplemented with 10% fetal bovine serum (FBS) and 1 × penicillin and streptomycin. YUMMER1.7 cells were grown in DMEM/F12 supplemented with 10% fetal bovine serum, 1 × penicillin and streptomycin and 1x non-essential amino acids. Primary BMDMs were maintained in DMEM supplemented with 10% FBS, 1% penicillin/streptomycin and 1ng/ml M-CSF1. All cells were cultured at 37 °C in 5% CO_2, and routinely tested for mycoplasma.

Gene disruption by CRISPR/Cas9

For *Adar* ablation, immortalized MEFs were transiently transfected with TrueGuide Synthetic sgRNA against mouse *Adar* (Thermo Fisher Scientific, CRISPR162007_SGM) and TrueCut Cas9 Protein (Thermo Fisher Scientific, A36499) by Lipofectamine CRISPRMAX Cas9 Transfection Reagent (Thermo Fisher Scientific, CMAX00008). After two days, cells were harvested and examined for ADAR1 protein expression by

immunoblotting. To ablate *Mavs*, immortalized MEFs were infected with *Mavs* sgRNA-expressing 'all-in-one' lentivirus (Abmgood, Cat. 281531140502) followed by selection in puromycin (5 μg/mL) for five days.

Immunofluorescence microscopy

Cells were plated on 8-well glass slides (EMD Millipore), and allowed to adhere for at least 24 hrs before use in experiments. Following treatment, cells were fixed for 10 min with freshly-prepared 4% (w/v) paraformaldehyde in PBS, permeabilized in 0.5% (v/v) Triton X-100 in PBS, blocked with MAXblock™ Blocking Medium (Active Motif), and incubated overnight with primary antibodies at 4°C. After three washes in PBS, slides were incubated with fluorophore-conjugated secondary antibodies for 1 hr at room temperature. Following an additional three washes in PBS, slides were mounted in ProLong Gold antifade reagent (Thermo Fisher Scientific) and imaged by confocal microscopy on a Leica SP8 instrument. For immunofluorescence staining of tumors, frozen tumor sections were cut at 10 μm thickness in a cryostat microtome. Sections were permeabilized with 0.5% (v/v) Triton X-100 in PBS, blocked with MAXblock™ Blocking Medium (Active Motif), and incubated overnight with primary antibodies at 4°C. After three washes in PBS, slides were incubated with fluorophore-conjugated secondary antibodies for 1 hr at room temperature. Following an additional three washes in PBS, slides were mounted in ProLong Gold antifade reagent (Thermo Fisher Scientific) and imaged by confocal microscopy on a Leica SP8 instrument. Fluorescence intensity was quantified using Leica LAS X software. When required, RNase A (1mg/mL) or DNase I (25 U/mL) was used for 1 hr at 37 °C before primary antibody incubation. Primary antibodies were used for immunofluorescence studies: Z-DNA and Z-RNA (clone Z22, Absolute Antibody), A-RNA (clone 9D5, Millipore), phosphorylated murine MLKL (Cat. 37333, Cell Signaling); clone 7C6.1, Millipore [MABC1158] or gift from Dr. Douglas R. Green), FLAG (Cat.A00187, GenScript), Lamin B1 (ab16048, Abcam), PDGFRα (Cat. 14-1401-82, Thermo Fisher Scientific), CD3 (PE-CF594, Clone: 53-6.7, eBioscience), CD8 (FITC, Clone: 145-201, eBioscience), CD44 (15675-1-AP, Proteintech), GmzB (ab255598, Abcam), Ki67 (MA5-14520, Thermo Fisher Scientific), CD11c (Cat. 14-0114-85, Thermo Fisher Scientific), F4/80 (NB600-404, Novus Biologicals).

RNA immunoprecipitation (RIP)-seq

Cells were treated with or without IFNβ for 48 hrs, harvested, and RIP conducted using the Magna RIP RNA-Binding Protein Immunoprecipitation Kit (Millipore) following the manufacturer's instructions. Briefly, cell pellets were lysed in RIP lysis buffer, followed by incubation with RIP Buffer containing magnetic beads conjugated with Z-RNA or isotype control antibody at 4°C overnight. Samples were then incubated with proteinase K and immunoprecipitated RNAs were recovered by phenol:chloroform:isoamyl alcohol purification. RNA was quantified using the Quant-iT RiboGreen RNA assay (Thermo Fisher Scientific) and assessed for quality with the 2100 Bioanalyzer RNA 6000 Nano assay (Agilent) or 4200 TapeStation High Sensitivity RNA ScreenTape assay (Agilent) prior to library generation. Libraries were prepared from total RNA with the TruSeq Stranded Total RNA Library Prep Kit according to the manufacturer's instructions (Illumina, PN 20020599). Libraries were analyzed for insert size distribution using the 2100 BioAnalyzer High Sensitivity kit (Agilent), 4200 TapeStation D1000 ScreenTape assay (Agilent), or

5300 Fragment Analyzer NGS fragment kit (Agilent). Libraries were quantified using the Quant-iT PicoGreen ds DNA assay (Thermo Fisher Scientific) or by low pass sequencing with a MiSeq nano kit (Illumina). Paired-end 150 cycle sequencing was performed on a NovaSeq 6000 (Illumina).

Quantitative PCR

RNA from RIP samples was reverse-transcribed into cDNA using Superscript IV VILO Master Mix (Thermo Fisher Scientific). cDNA or DNA from ChIP samples was used as template and quantitative PCR was performed using SYBR Green (Thermo Fisher Scientific). Primers used were as follows:

Xrn1-fwd: GTTAGAAATTACTGATAGCTGG

Xrn1-rev: GACAGGGTTTCTCTGTGTAG

Knl1-fwd: AGATCAGCCCAGGCTATACAG

Knl1-rev: AATAGCAAGCAGATAACATGC

Slfn5-fwd: CTCATTTGTCATTTGCTTTAGG

Slfn5- rev: AAGTTTGCTCTGTTTGGCTC

Isg15-fwd: AGTGATGCTAGTGGTACAGAACT

Isg15-rev: CAGTCTGCGTCAGAAAGACCT

Eif2ak2-fwd: AGCTCCAAATAACCAAGATAC

Eif2ak2-rev: CTCTGCTCTACACTCTATCTCC

Ddx58-fwd: GAATGCACTCTGTAGTCCAG

Ddx58-rev: ATAAATGAAAGTCAGCTCTCAG

Ifih1-fwd: GGAATGCCCATGAGGTATTG

Ifih1-rev: AGCTTGCCACATTGCATTG

L1Md A-fwd: ACATAGGGAAGCAGGCTACCC

L1Md A-rev: GGCAAGACTCTGCTGGCAAGG

L1Md T-fwd: AAGCACAGAGGCGCTGAGGCAG

L1Md T-rev: GACTAATTTCCTAAGTTCGGC

Circular Dichroism

CD experiments were performed on a Jasco model J-820 CD spectrophotometer. Dumbbell RNA [r(CACACUUGUGUGCUUCACACUUGUGUG)] and control RNA

[r(CCUUCUUGAAGGCUUCCUUCUUGAAGG)] were prepared at 10 μM in 10 mM Tris-HCl buffer (pH 7.0) in the presence of 3 M NaCl at 10°C. For CBL0137 and Z-DNA binding assay, [d(Cm8mGCACm8mGCG)/d(CGCGTGCG)] DNA was prepared at 9.4 μM in 100mM NaCl and 5mM Na-PO4 buffer (pH 7.0). CBL0137 was added into the DNA solution and kept at room temperature for 30 min before measurement.

In Situ Proximity Ligation Assay

Cells were fixed with freshly prepared 4% (w/v) paraformaldehyde in PBS for 10 min, permeabilized in 0.5% (v/v) Triton X-100 in PBS for 15 min, and subjected to *in situ* proximity ligation assay according to the manufacturer's instructions (Sigma-Aldrich, Duolink™ In Situ Red Starter Kit Mouse/Rabbit).

Chromatin Immunoprecipitation (ChIP)-seq

Immortalized MEFs treated with or without CBL0137 were subjected to ChIP using the EZ-Magna ChIP HiSense Chromatin Immunoprecipitation Kit (Millipore) following the manufacturer's instructions. Briefly, cells were cross-linked by 1% formaldehyde (in DMEM). Nuclei were isolated by Nuclei Isolation Buffer. The cross-linked DNA was sheared to 200-500 base pair in length by sonication. Sheared DNA was immunoprecipitated using anti-Z-DNA, FLAG or isotype control antibody at 4°C overnight. Library preparation and paired-end 150bp DNA sequencing was performed by Novogene.

^{19}F NMR measurement

Z-DNA d(CGC^{F}GCG)$_2$ was prepared at 50 μM in 10 mM NaCl and 1 mM Na-PO4 buffer (pH 7.0). CBL0137 was added into the Z-DNA solution and kept at room temperature for 30 min before measurement. The ^{19}F NMR spectrum was measured on a Bruker AVANCE 400 MHz spectrometer at a frequency of 376.05 MHz and referenced to the internal standard CF3COOH (−75.66 ppm)[3].

Immunoprecipitation and immunoblotting

Immortalized *Zbp1*$^{-/-}$ MEF populations stably reconstituted with FLAG-tagged WT or empty vector (Vec) were lysed in IP lysis buffer (Thermo Fisher Scientific) supplemented with protease and phosphatase inhibitors (Thermo Fisher Scientific). Cell lysates were incubated on ice for 10 min, and briefly sonicated to shear chromatin, then cleared by high-speed centrifugation (20,000*g*, 10 min) at 4°C. After saving 5% of the total cell lysate for input, the extracts were subjected to immunoprecipitation with anti-FLAG M2 affinity gel, according to the manufacturer's instructions (Sigma). Resin was eluted with 3×FLAG peptide, and the supernatants were subjected to immunoblot analysis as described previously[4]. Sources and dilutions of primary antibodies were as follows: ADAR1 (sc-73408, Santa Cruz Biotechnology, 1:1000), phosphorylated murine MLKL (Ab196436, Abcam, 1:2000), phosphorylated human MLKL (#91689, Cell Signaling Technology, 1:1000), total murine MLKL (MABC60, EMD Millipore, 1:2000), total human MLKL (#14993, Cell Signaling Technology, 1:2000), RIPK3 (#2283, ProSci, 1:2000), FLAG (A00187, GenScript, 1:2000), MAVS (sc-365334, Santa Cruz Biotechnology, 1:1000), ADAR2 (sc-73409, Santa Cruz Biotechnology, 1:1000), phosphorylated STAT1 (#9167, Cell

Signaling Technology, 1:2000), total STAT1 (#9172, Cell Signaling Technology, 1:2000), RIPK1 (#610459, BD Transduction Laboratories, 1:2000), FADD (ab124812, Abcam, 1:2000), Caspase 8 (#9746, Cell Signaling Technology, 1:2000), GAPDH (#60004-1-Ig, Proteintech, 1:4000).

The Cancer Genome Atlas (TCGA) data analysis

RSEM-normalized gene expression for melanoma (TCGA-SKCM)[5] was obtained from the Broad Institute Firehose pipeline (Data version 2016_01_28). Microenvironment cell population counter analysis[6] was used to estimate tumor infiltrating populations. Log_2 transformed data was used as input. Heatmaps were plotted using the pheatmap package available in Bioconductor (https://cran.r-project.org/web/packages/pheatmap/index.html). All calculations were done in the R programming environment.

Single Cell RNA (scRNA)-seq data analysis

scRNA-seq data from Ishizuka *et al.* (GSE110746)[7] were analyzed using the Cell Ranger analysis pipeline (v1.2), as described previously[8]. Downstream analyses and violin plots were generated using Seurat package[9]. The clusters were classified as in the Ishizuka *et al.* study.

Mouse melanoma models

Mice were anesthetized, shaved at the injection site, and 5×10^5 B16-F10 cells or 2×10^6 YUMMER1.7 cells were subcutaneously injected in the right flank. Tumors were measured every two days once palpable with a caliper. Tumor volume was calculated using the formula $0.5\times D\times d^2$ where 'D' is the longer diameter and 'd' is the shorter diameter. Treatment was initiated when mean tumor size was ~100 mm^3 for B16-F10 tumors or ~150 mm^3 for YUMMER1.7 tumors. 50 μl CBL0137 or vehicle was delivered via intratumoral injection and 200 μmg anti-PD-1 antibody (clone RMP1.14, Bio X cell) or isotype control IgG (clone 2A3, Bio X cell) was delivered via intraperitoneal injection. Treatment was performed every two days for a total of 4 doses. Mice were euthanized when tumors reached defined endpoints (volume greater than or equal to 2000 mm^3 for B16-F10 tumors or 1000 mm^3 for YUMMER1.7 tumors), or when ulceration or bleeding of tumors was observed. For studies in the B16-OVA melanoma model, 2×10^6 B16-OVA cells were subcutaneously injected on the right flank, or equivalently on both right and left flanks for the bilateral tumor model used in studies examining abscopal effects of CBL0137. Treatment was initiated when the tumor volume reached ~100 mm^3. For flow cytometry, tumor draining (inguinal) lymph nodes (tdLNs) were harvested after 4 doses of treatment. Leukocytes were isolated from tdLNs by mashing over a 70 μm cell strainer in PBS. Leukocytes were counted and 1×10^6 cells were plated into a V-bottom 96-well plates for antibody staining. Cells were first incubated with OVA tetramers (SIINFEKL H-$2K^b$) at 1:200 dilution for 1 hr at room temperature, before washing and incubated with antibodies (anti-CD45, anti-CD3, anti-CD8) for 45 minutes at 4°C. All antibodies were used at a 1:200 dilutions in 1% FBS/ 0.1% NaN_3/PBS. Cells were pelleted, washed, and resuspended for data collection on a BD FACSymphony A5 flow cytometer and analyzed using FlowJo v10 software. Percentages of specific cell populations were determined using FlowJo and combined with cell counts to establish total cell numbers. The following antibodies or tetramers were used for flow

cytometry: SIINFEKL H-2K^b tetramer-APC (BioLegend, Cat# 141606), SIINFEKL H-2K^b tetramer-PE (BioLegend, Cat# 141604), anti-CD45 APC-Cy7 (BioLegend, Cat# 103116), anti-CD3 Pacific Blue (BioLegend, Cat# 100214) and anti-CD8 FITC (MBL, Cat# D271-4).

RIP-seq Analyses

Alignment and filtering of RNAs: Initial processing of FASTQ files was accomplished using the nf-core/rna-seq (v.3.0) bioinformatics pipeline (DOI: 10.5281/zenodo.3503887). Sequences were aligned to the mm10 assembly and filtered to remove supplementary and secondary alignments, as well as reads that failed to map in proper pairs. Ribosomal reads were also marked and excluded.

Identifying IFNβ stimulated genes (ISG) and RIP-enriched RNAs in ADAR1/ZBP1 null MEFs.—For transcriptome analysis, we used Salmon[10] gene-level quantifications and the DESeq2 (v1.34.0)[11] R package. All p-values were adjusted for multiple testing using the Benjamini-Hochberg method. A gene was categorized as an ISG if it manifested >1.5 fold-change in expression levels (p-adj < 0.01, one-sided test) at 24 or 48 hrs of IFNβ treatment. Additionally, we supplemented our data with early ISGs from WT cells (GSE118926[12], reanalyzed using the same pipeline and methodology), because after deletion of ADAR1, MEFs can initiate IFN production in response to endogenous A-RNAs. To identify RNAs enriched in RIP-Seq experiments, we compared RNAs from each antibody pulldown to their total cellular levels, measured by RNA-seq of input RNA. RNAs with fold change > 2 and p-adj < 0.01 (one-sided test) in antibody pulldowns, compared to their input levels, were classified as enriched.

Calculating Alu Editing Index (AEI).—The AEI pipeline[13] was used to summarize A→I editing frequency in Z22 RIP-seq from WT MEFs. The original AEI is a genome-wide editing measure and does not provide information at the level of individual genomic repeats. To localize ADAR1 editing substrates further, we focused on a similarly defined region-wise editing measure not limited to Alu/SINE elements. That is, for each repeat in the genome, editing index was calculated as the total number of A→G mismatches divided by the coverage of adenosines and multiplied by 100. Importantly, this is the same method as for estimating genome-wide AEI, but provides resolution at the level of individual repeats. Among all repetitive elements identified from RepeatMasker annotations, those with a mean coverage per adenosine site of more than 5 fragments and an editing index higher than 1% were selected for further consideration. These elements were manually verified using RNA folding prediction[14] and known editing sites from the REDI portal[15] to exclude unannotated SNPs (100% T→C or A→G mismatches), high sequencing noise regions, and other false positive hits. A curated set of repeats was then mapped to the GENCODE annotation (VM25) using the HTSeq package (0.12.3)[16].

ChIP-seq Analyses

Raw fastq files were preprocessed using an in-house pipeline, comprising four major stages: (1) read trimming; (2) alignment to the reference genome; (3) duplicate identification and filtering, and (4) quality control.

Read trimming.—Adapters and low-quality base pairs were trimmed using the Trim Galore[17] program (v0.6.5). Specifically, flanking sequences that had at least 5 bp overlap with known adapters were removed, and reads trimmed using a Phred threshold of 20.

Alignment.—The trimmed reads were aligned to the mm10 mouse reference genome assembly using minimap2 aligner (v2.17)[18]. The alignment parameters used were the default recommendations for short paired-end libraries.

Duplicate identification and filtering.—Duplicate fragments were marked using SAMtools (v1.7)[19]. Libraries were then filtered to remove duplicates, reads that failed to form proper pairs, supplementary and secondary alignments.

Quality control.—The quality of libraries was assessed by the total number of usable fragments and ENCODE library complexity metrics (NRF, PBC1, PBC2). Each experiment had at least 15 million (mln) usable fragments (30 mln on average) and acceptable values for most of the library complexity metrics as defined by the ENCODE (i.e., NRF ≥ 0.5, PBC1 ≥ 0.5, PBC2 ≥ 1).

Enrichment peaks were identified using MACS2 (v2.2.6)[20] with default parameters, except that fold enrichment cutoff was set to 2 and all duplicated fragments for technical replicates retained. MACS2 was used to build fold-enrichment signal tracks for Z22 and FLAG-ZBP1 datasets, as described in the ENCODE3 ChIP-seq pipeline (v1). Peaks with at least 1bp overlap with ENCODE blacklisted genomic regions were excluded from further analysis.

Annotation of Z22 peaks.—Z22 peaks were mapped against known repetitive sequences using a custom Python script and the RepeatMasker annotation downloaded from the UCSC Table Browser. Specifically, each peak was assigned a unit weight, which then was distributed between the repeats overlapping it in proportion to the length of the intersection. That is, the peak covered by a LINE-1 repeat by 30% contributes 0.3 to the "LINE-1" category and 0.7 to the "repeats-free" category. RepeatMasker annotation was used to calculate the total genomic coverage for the major repeat families. ENCODE blacklisted regions were reported separately. L1Md A and L1Md T repeats having at least a 1 bp overlap with Z22 peaks were mapped to known genes using, ChIPpeakAnno (v3.0.0)[21] with the ENSEMBL annotation package (TxDb.Mmusculus.UCSC.mm10.ensGene, v3.4.0). A Circos[22] plot showing the distribution of these repeats in the genome is provided in the Extended data Figure 4d.

Comparison of Z22 and FLAG-ZBP1 peaks.—The initial comparison of Z22 and FLAG-ZBP1 distribution of peaks was carried out using the whole-genome Circos plot with three separate tracks: two for peaks (q-value threshold 0.05) and one for their overlap. For a quantitative analysis, shared peaks were defined as having an intersection of at least 1 bp, and the total number of such peaks within ORF1- and ORF2-intact LINE-1 repeats was calculated based on the L1Base[23] annotation. The L1Base annotation was also used to calculate the percentage of LINE-1 elements in each L1Base category that overlapped with Z22 and FLAG-ZBP1 peaks. Each repeat was assigned to the single most descriptive class;

for example, a completely intact LINE-1 element was only counted in the ‘ORF1 & ORF2 intact’ category but not in the ‘ORF2 intact’ category.

Building enrichment profiles for L1Md A and L1Md T repeats.—We define the enrichment profile as a model, allowing one to visualize the aggregated distribution of fold enrichment values for a given set of repeats. Such profiles are helpful in understanding the binding patterns of Z22 and FLAG-ZBP1 in intact L1Md A and L1Md T repeats. In general, the construction of an enrichment profile consists of four steps: (1) build a consensus sequence for the repeats of interest; (2) align individual repeats to the consensus; (3) calculate mean enrichment based on the alignment of repeat sequences present in the reads from the pull-down experiments; (4) smooth the aggregated enrichment values. An example of the procedure for L1Md A repeats is provided in the Extended data Figure 7. In our case, a consensus sequence for L1Md A repeats was built based on the multiple alignments of the ORF1 and ORF2 of intact L1Md A elements that are of length 6000 to 7000 bases. Clustal Omega (v1.2.4)[24] was used for alignment, and the consensus was composed of the most frequent nucleotides in alignment positions with over 50% occupancy. To construct the profile, only L1Md A elements with intact ORF1 and ORF2 and having at least 1 bp overlapping with Z22 and FLAG-ZBP1 peaks were used. A triangular window of length 8 bp with weights proportional to the number of matched positions was employed to smooth the profiles. The same method was utilized for the L1Md T repetitive elements. Finally, the NCBI ORFfinder online tool (Open Reading Frame Finder; RRID:SCR_016643) was used to annotate consensus sequences. Identified ORF1 and ORF2 were tested using BLAST to ensure that they encode the known LINE-1 proteins.

Co-localization of Z22/FLAG peaks and Z-DNA prone sequences in L1Md A and L1Md T repeats.—The Z-Hunt[25] program was used to examine the propensity of L1Md A and L1Md T elements bound by Z22/FLAG-ZBP1 to form Z-DNA. Z-Hunt is based on experimentally determined thermodynamic properties of DNA and predicts the Z-propensity score (Z-score) for short DNA windows (~10 nucleotides). The score is defined as the inverse of the probability of finding an as-good or better Z-forming sequence in a collection of random DNA segments of the same length. In summary, Z-Hunt allows us to estimate the potential of each subsequence in L1 repeats to form Z-DNA. First, for each repeat intersecting with Z22 peaks, its best ZH-scoring window was mapped to the consensus annotation. Specifically, each L1 element was aligned to its consensus, as described above, and then assessed for whether the best ZH-scoring subsequence falls within 5’UTR, ORF1, ORF2, or 3’UTR. In cases of multiple equally scored windows mapped to different segments, fractional counts were used. That is, if in a given repeat the best ZH-scoring sub-sequence is in 5’UTR and ORF1, these segments were assigned 1/2 weight. Overall, the vast majority (~90%) of the best Z-forming windows are within the 5’UTR, which is consistent with the enrichment profiles. Next, for L1 elements with intact ORF1 and ORF2, and where Z22- and FLAG-enrichment summits were in the 5’UTRs, a joint enrichment summit was defined as a location in the 5’UTR where the sum of L1-normalized Z22 and FLAG enrichment values is maximum. Here, the MACS2 fold enrichment tracks were used, as detailed earlier, and L1-normalization refers to the mathematical L1 vector normalization. Z-Hunt was then employed for each repeat and a ±150bp window around

its enrichment summit. The top-scoring subsequence for each repeat was select, and in the case of multiple windows with identical scores, the closest to the joint summit was preferred. Overall, 72% of the subsequences with the best ZH-scores were found within a ±150 bp enrichment summit window. Notably, this region contains a bidirectional promoter driving transcription of ORF1 and a spliced transcript called ORF0 that is not annotated by the NCBI ORFfinder online tool[26]. Among these windows, the "CAATCGCGCGGA" (ZH-score ≈ 241; with the ZH-Score for “CGCGCG” ≈ 884) was overrepresented in L1Md A elements (98.1% subsequences near the joint enrichment peak), "CAGGTGCCCGCCCG" (ZH-score ≈ 198) and "GCACAGGCGCCGGC" (ZH-score ≈ 236) in L1Md T elements (70.2% and 22.3% subsequences near the joint enrichment peak).

Feature importance analysis by DeepZ

Data preparation.—Genome assembly MGSCv37 (mm9) was used for the feature analysis and subsequently verified using mm10. All epigenomic data were collected from Chip-atlas[27]. Three different data sets of Z-DNA peaks were used as targets: Z22 peaks, FLAG-ZBP1 peaks, and their union. For each dataset, the feature analysis was performed independently, and the results were subsequently compared. All datasets were mapped to the mm9 reference using the UCSC genome browser LiftOver tool to ensure consistency with ChIP-Atlas results. The whole pipeline of epigenomics data and DNA sequence preparation is described in Beknazarov et al[28], where each nucleotide can be associated with a vector of 874 epigenomic features, as well as with a Z-Hunt score. Depending on the dinucleotide (a base and the nucleotide immediately following it), the feature takes the value 0 or −1, where −1 penalizes dinucleotide with a low probability of Z-formation under physiological conditions (AA, TT, TA, AT, AC, GA, AG, GC, GT, CT, TC) and 0 otherwise (CG, CA, TC, CC, GG).

Model selection and interpretation.—Training data sets were created the same way as in Beknazarov et al[28]. Logistic regression with L2 regularization was chosen as the predictive model for its ease of interpretation and good quality on all 3 datasets. For consistency with DeepZ, the linear model was implemented as a neural network with one output and one fully connected layer. The importance of the features is represented by linear regression weights if the features initially have the same spread of values. Since all the features in our dataset have the same range, the weights of the linear model can be used without additional processing.

Extended Data

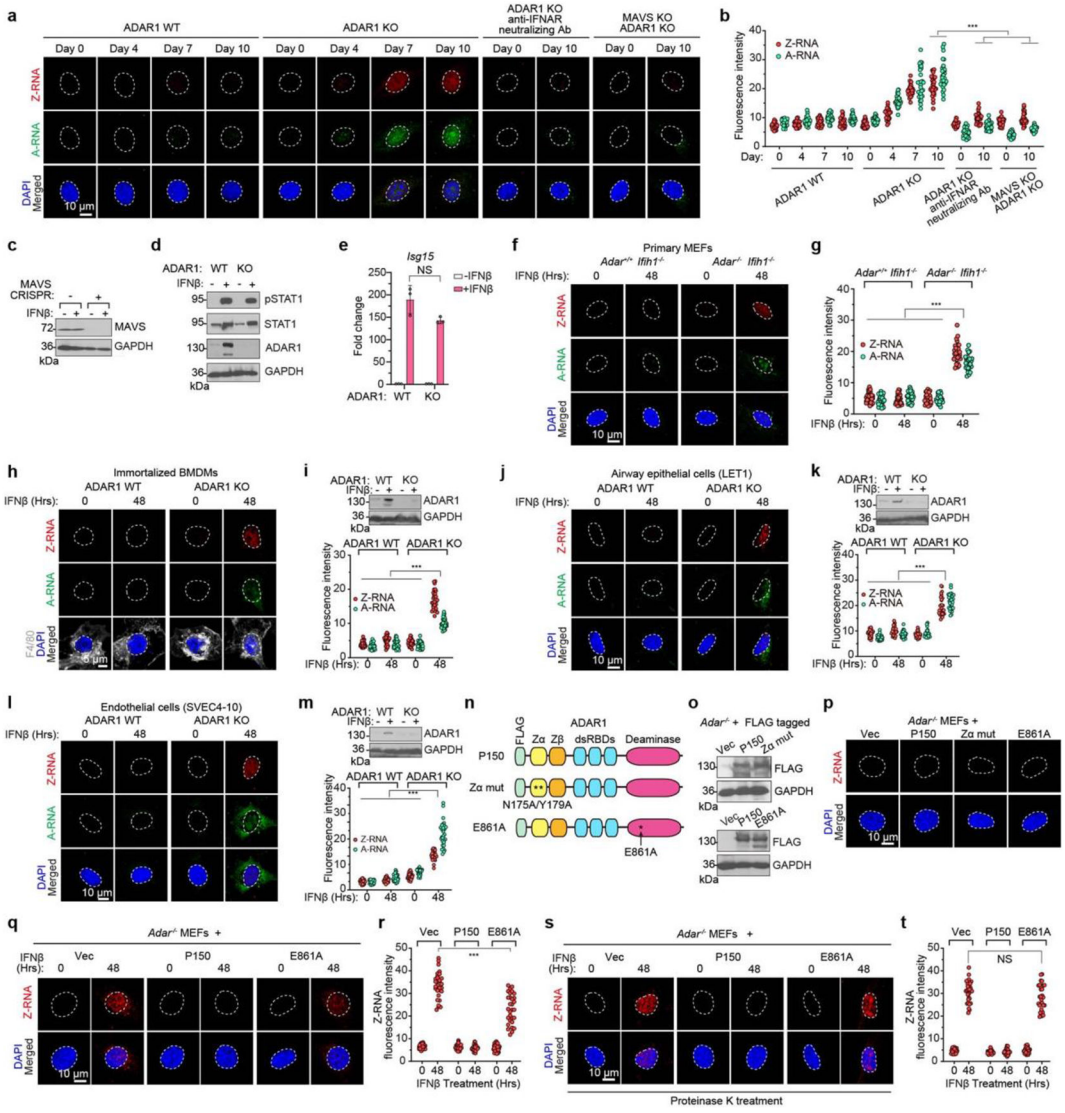

Extended Data Fig. 1. Z-RNA accumulation upon *Adar* ablation.

a, Time course of Z-RNA and A-RNA formation in ADAR1 WT, ADAR1 KO, ADAR1/MAVS double KO MEFs, or ADAR1 KO MEFs treated with anti-IFNAR1 neutralizing antibody (20 μg/mL). **b**, Quantification of fluorescence intensity of Z-RNA and A-RNA signals in **a**. **c**, MAVS protein levels in WT MEFs following CRISPR-based murine *Mavs* (MAVS KO), and exposure to IFNβ (100 ng/mL, 24 hrs). *Mavs* was ablated using lentiviruses expressing 'all-in-one' sgRNA. **d**, Whole-cell extracts from ADAR1 WT or ADAR1 KO treated with IFNβ for 6 hrs were examined for phosphorylated STAT1, total STAT1 and ADAR1 by immunoblot analysis. **e**, *Isg15* mRNA levels were examined by RT-qPCR in ADAR1 WT or ADAR1 KO treated with or without IFNβ for 6 hrs. **f**, Detection of Z-RNA and A-RNA accumulation in primary $Adar^{+/+}Ifih1^{-/-}$ or $Adar^{-/-}Ifih1^{-/-}$ MEFs in the presence or absence IFNβ (100 ng/mL). **g**, Quantification of fluorescence intensity of Z-RNA and A-RNA signals in **f**. **h**, Detection of Z-RNA and A-RNA accumulation in

immortalized BMDMs in the presence or absence of IFNβ (100 ng/mL), following ADAR1 ablation by CRISPR-based approaches. **i**, Protein levels of ADAR1 p150 in immortalized BMDMs were detected by immunoblot (upper panel). Quantification of fluorescence intensity of Z-RNA and A-RNA signals in **h** (bottom panel). **j**, Detection of Z-RNA and A-RNA accumulation in airway epithelium-derived immortalized LET1 cells in the presence or absence of IFNβ (100 ng/mL), following ADAR1 ablation by CRISPR-based approaches. **k**, Protein levels of ADAR1 p150 in LET1 cells were detected by immunoblot (upper panel). Quantification of fluorescence intensity of Z-RNA and A-RNA signals in **j** (bottom panel). **l**, Detection of Z-RNA and A-RNA accumulation in ADAR1 WT or KO immortalized endothelial SVEC4-10 cells in the presence or absence of IFNβ (100 ng/mL). **m**, Protein levels of ADAR1 p150 in SVEC4-10 cells were detected by immunoblot (upper panel). Quantification of fluorescence intensity of Z-RNA and A-RNA signals in **l** (bottom panel). **n**, Schematic of FLAG-tagged ADAR1 p150, E861A and Zα (N175A/Y179A) mutants used in this experiment. **o**, Equivalent expression levels of ADAR1 constructs in stably-reconstituted *Adar*$^{-/-}$ MEFs were confirmed by immunoblotting. **p**, Z-RNA accumulation in immortalized *Adar*$^{-/-}$ MEFs stably reconstituted with empty vector (Vec), or with ADAR1 p150, Zα N175A/Y179A (Zα mut) or editing-deficient (E861A) mutants without IFNβ treatment. **q**, Detection of Z-RNA accumulation in ADAR1 p150 or E861A mutant cells following IFNβ (100 ng/mL) treatment. **r**, Quantification of fluorescence intensity of Z-RNA signals in **q**. **s**, Detection of Z-RNA accumulation in ADAR1 p150 or E861A mutant cells after proteinase treatment. Fixed cells were treated with proteinase K (0.008 U/ml) for 30 min before staining. **t**, Quantification of fluorescence intensity of Z-RNA signals in **s**. Data are mean ± s.d. (n = 30 in **b**, **g**, **i**, **k**, **m**, **r**, **t** or n = 3 in **e** per group). One-way ANOVA test (**b**, **g**, **i**, **k**, **m**), two-tailed unpaired t-test with Welch's correction (**e**, **r**) or two-tailed unpaired Student's t-test (**t**). ***$P < 0.0005$ ($P < 0.0001$ in **b**, **g**, **i**, **k**, **m**, **r**). NS, no significance. Data are representative of at least three independent experiments. *Adar* was ablated by CRISPR-based approaches, as detailed in the manuscript.

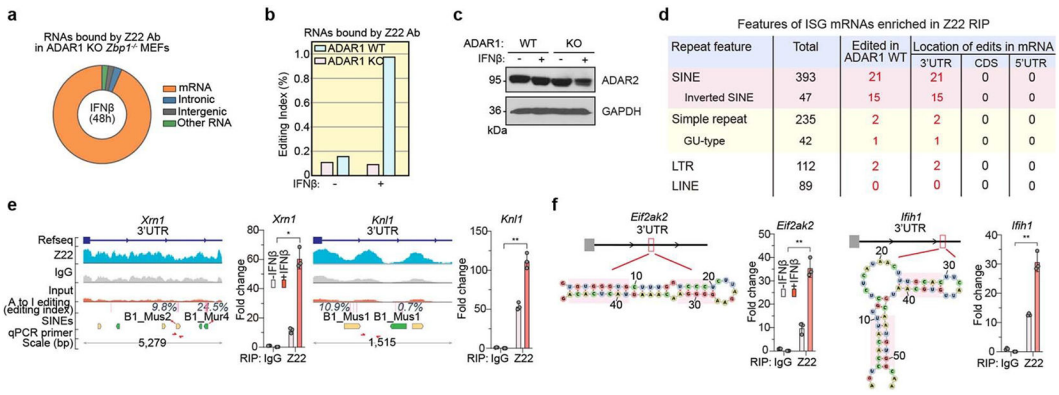

Extended Data Fig. 2. Z-forming mRNAs suppressed by ADAR1.

a, Origin of sequenced RNA fragments in Z22 RIP-seq for ADAR1 KO *Zbp1*$^{-/-}$ MEFs with IFNβ (100 ng/mL). **b**, A→I Editing Index of RNAs in Z22 pull-downs from ADAR1 WT and ADAR1 *Zbp1*$^{-/-}$ KO cells before and after IFNβ treatment (100 ng/mL). **c**, Expression levels of ADAR2 in ADAR1 WT or ADAR1 KO MEFs in the presence or absence of IFNβ (100 ng/mL, 24 hrs). **d**, Distribution of repeats in Z22 enriched ISG mRNAs from ADAR1

KO *Zbp1*$^{-/-}$ MEFs. Localization and the total number of repeats that were also edited in Z22 pulldowns from IFNβ-treated ADAR1 WT cells are provided in red (A→I Editing Index > 0.1%; mean coverage per adenosine > 5). **e**, 3'UTRs of inverted SINE-containing mRNAs showing Z22 enrichment (blue peaks), IgG (grey peaks), input (orange peaks), editing sites (vertical red bars), location of SINEs, and location of qPCR primers (red arrows). qPCR quantitation of the indicated inverted SINE-containing mRNAs (*Xrn1* and *Knl1*) 3'UTRs following immunoprecipitation with Z22 or control IgG antibodies from ADAR1 MEFs stimulated with or without IFNβ (100 ng/mL, 48 hrs) is shown to the right. **f**, qPCR analysis of the indicated GU-type simple repeat containing mRNAs (*Eif2ak2* and *Ifih1*) following immunoprecipitation with Z22 or control IgG antibodies from ADAR1 KO MEFs. Potential bipartite (dumbbell) Z-forming RNA structures (RNA-fold) are shown to the right of each graph, and putative Zα binding sites are outlined in pink boxes. Data are mean ± s.d. (n = 3 in **e**, **f** per group). Two-tailed unpaired t-test with Welch's correction (**e**, **f**). *$P < 0.05$ [$P = 0.005$ in **e** (*Xrn1*)], **$P < 0.005$ [$P = 0.003$ in **e** (*Knl1*), $P = 0.001$ in **f** (*Eif2ak2*), $P = 0.004$ in **f** (*Ifih1*)]. Data are representative of at least three independent experiments.

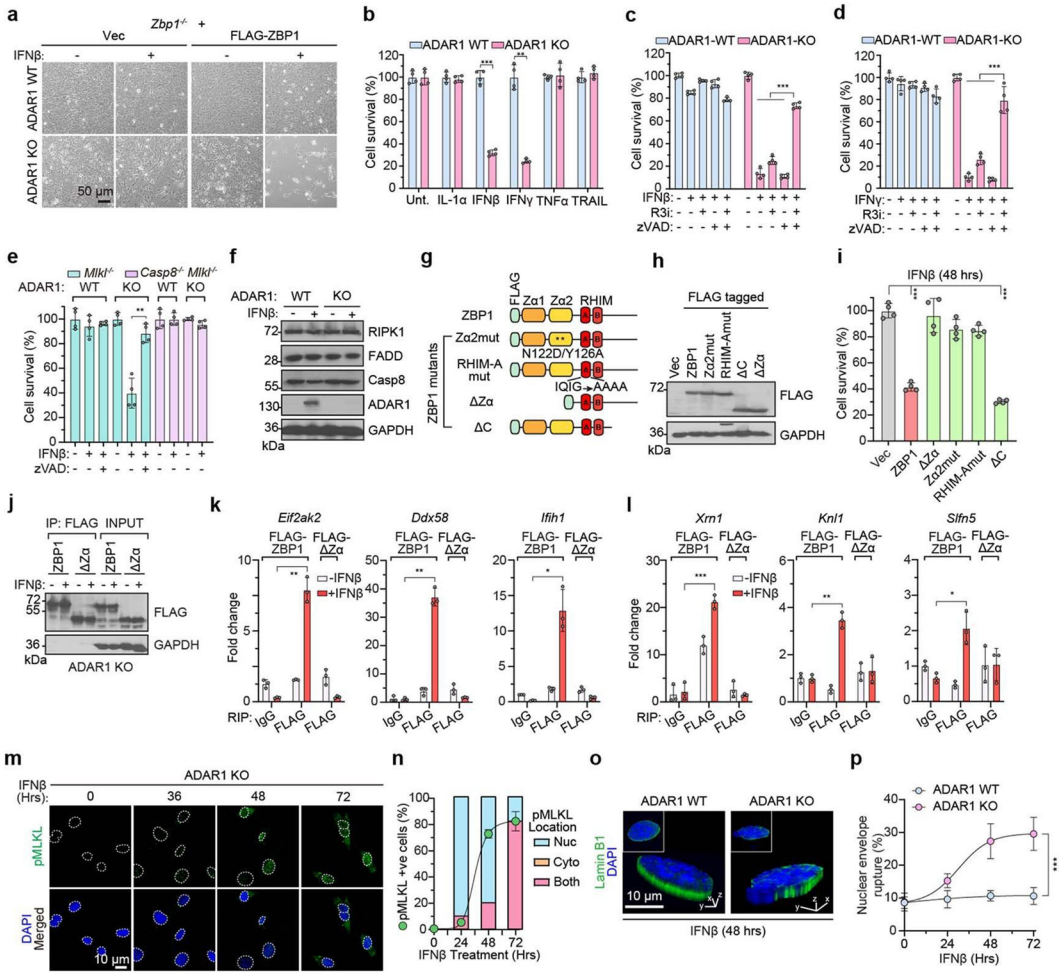

Extended Data Fig. 3. ZBP1-activated cell death following *Adar* ablation.

a, Photomicrographs of ADAR1 WT or ADAR1 KO following treatment with IFNβ (100 ng/mL, 48 hrs). **b**, *Zbp1*$^{-/-}$ MEFs stably expressing FLAG-ZBP1, in which ADAR1 was present (ADAR1 WT) or ablated by CRISPR/Cas9 (ADAR1 KO), were treated with the indicated cytokines (100 ng/mL). Cell viability was determined at 48 hrs post treatment. (**c**, **d**), MEFs produced as in **b** were treated with IFNβ (**c**) or IFNγ (100 ng/mL) (**d**) in the presence or absence of zVAD (50 mM) and RIPK3 inhibitor (R3i) GSK'843 (5 μM). Viability was examined at 48 hrs post treatment. **e**, *Adar* was ablated by CRISPR-based approaches in *Mlkl*$^{-/-}$ or *Mlkl*$^{-/-}$*Casp8*$^{-/-}$ MEFs. Cells were treated IFNβ (100 ng/mL) in the presence or absence of zVAD (50 mM). Viability was examined at 48 hrs post treatment. **f**, IFNβ (100 ng/mL)-treated ADAR1 WT and ADAR1 KO MEFs were lysed at 24 hrs post treatment and examined for RIPK1, FADD, Caspase 8 (Casp8), and ADAR1 by immunoblotting. **g**, Schematic of FLAG-tagged murine ZBP1 and its mutants. **h**, Equivalent expression levels of FLAG-ZBP1 constructs in retrovirally-reconstitued *Zbp1*$^{-/-}$ MEFs were confirmed by immunoblotting for the FLAG tag. **i**, Cell viability of *Zbp1*$^{-/-}$ MEFs stably expressing FLAG-ZBP1 or its mutants **e** was determined at 48 hrs post IFNβ (100 ng/mL) treatment. **j**, Immortalized *Zbp1*$^{-/-}$ MEFs stably reconstituted with either FLAG-ZBP1 or FLAG-ZBP1ΔZα mutant were ablated for ADAR1 expression by a CRISPR-based approach, treated with IFNβ (100 ng/mL, 48 hrs). Following cell lysis, anti-FLAG immunoprecipitates were examined for FLAG. Whole-cell extract (5% input) was examined in parallel for FLAG. GAPDH was used as a loading control. **k**, *Zbp1*$^{-/-}$ MEFs stably expressing FLAG-ZBP1 or FLAG-ZBP1ΔZα mutant were ablated for ADAR1 expression, treated with or without IFNβ (100 ng/mL). RNA present in anti-FLAG or control IgG immunoprecipitates was subjected to RT-qPCR using primers for the 3'UTRs of *Eif2ak2, Ddx58, or Ifih1*. **l**, *Zbp1*$^{-/-}$ MEFs reconstituted with FLAG-ZBP1 or FLAG-ZBP1ΔZα were ablated for ADAR1 expression, treated with or without IFNβ (100 ng/mL). FLAG or control IgG immunoprecipitates from cell lysates were subjected to RT-qPCR using primers for the 3'UTRs of *Xrn1, Knl1* or *Slfn5*. **m**, Immunofluorescence staining for pMLKL (green) in *Zbp1*$^{-/-}$ MEFs stably expressing FLAG-ZBP1 and ablated for *Adar* (ADAR1 KO) at the indicated time point after treatment with IFNβ (100 ng/mL). Nuclei are stained with DAPI (blue) and outlined with dashed white lines. pMLKL is seen in the nucleus and cytoplasm of cells after IFNβ exposure. **n**, Line graph depicts the kinetics of pMLKL positivity, and bars show the localization of the pMLKL signal. **o**, Lamin B1 (green) staining for nuclear envelope integrity of ADAR1 WT or ADAR1 KO MEFs at 48 hrs post treatment with IFNβ (100 ng/mL). **p**, Kinetics of nuclear envelope breakdown in ADAR1 WT or ADAR1 KO MEFs after IFNβ (100 ng/mL) treatment. Data are mean ± s.d. (n = 4 in **b**, **c**, **d**, **e**, **i**, **n**, **p** or n = 3 in **k**, **l** per group). Two-tailed unpaired t-test with Welch's correction (**b**, **e**, **i**, **k**, **l**), one-way ANOVA test (**c**, **d**) or two-way ANOVA test (**p**). *$P < 0.05$ [$P = 0.0178$ in **k** (*Ifih1*), $P = 0.026$ in **l** (*Slfn5*)], **$P < 0.005$ [$P = 0.0007$ in **b** (IFNγ), $P = 0.001$ in **e**, $P = 0.0044$ in **k** (*Eif2ak2*), $P = 0.002$ in **k** (*Ddx58*), $P = 0.0018$ in **l** (*Knl1*)], ***$P < 0.0005$ [$P < 0.0001$ in **b** (IFNβ), **c**, **d**, **i**, $P = 0.0002$ in **l** (*Xrn1*)]. Data are representative of at least three independent experiments.

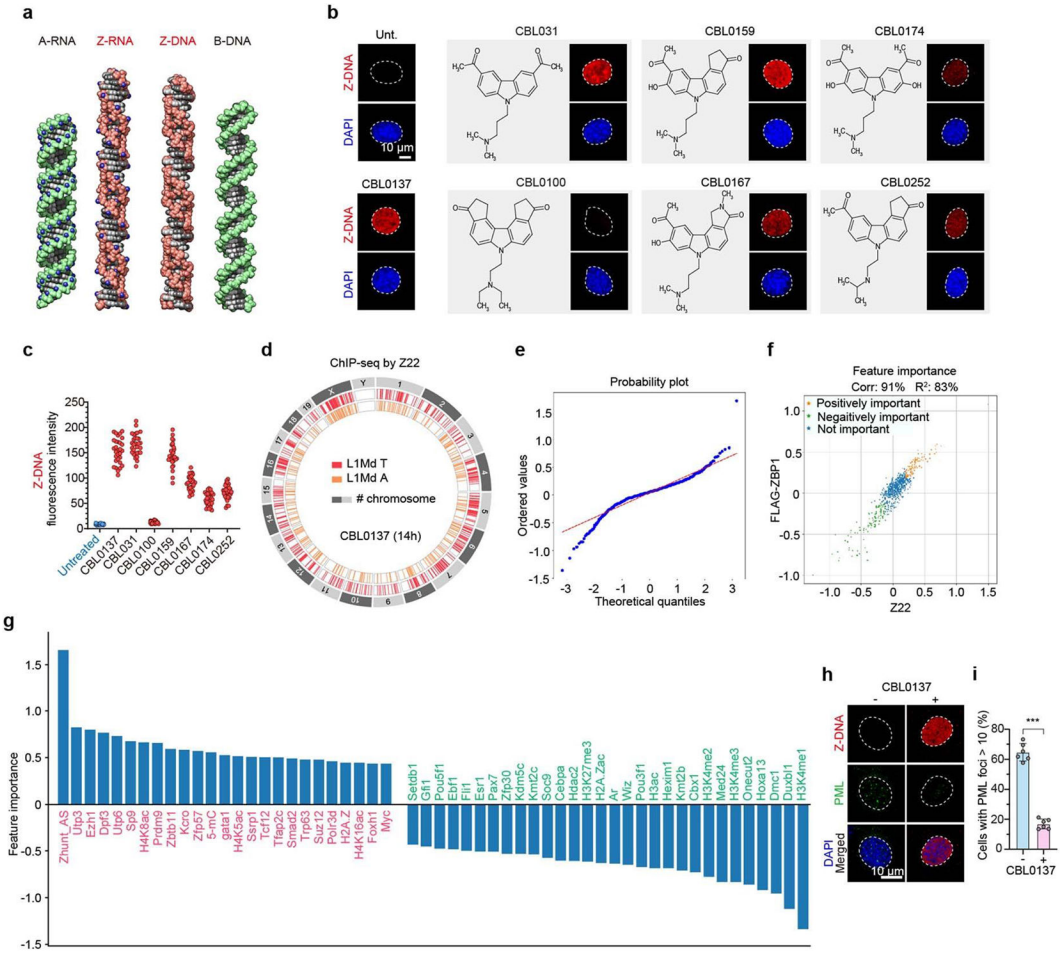

Extended Data Fig. 4. CBL0137 induced Z-DNA formation.

a, Structures of A-RNA, Z-RNA, Z-DNA and B-DNA. **b**, Z-DNA inducing activity of CBL0137 analogs. **c**, Quantification of fluorescence intensity of Z-DNA signal in **b**. **d**, Genomic distribution of L1Md A and L1Md T repeats overlapping with Z22 peaks in CBL0137-treated FLAG-ZBP1 MEFs. **e**, Quantile-quantile plot of the linear model weights for the features analyzed by DeepZ. The graph shows that the values for the upper and lower bounds of the plot differ from the normal distribution expected under the null hypothesis. **f**, Comparative plot of the importance of the features evaluated in datasets Z22 and FLAG-ZBP1 shows the reproducibility of the DeepZ analysis when each independently derived data set was analyzed separately. **g**, The importance of features based on the weights of linear regression trained on the combined Z22 and FLAG-ZBP1 dataset are scored using a normalized scale of 1 to −1. Epigenetic marks, transcription factor binding sites and other elements that predict pull-down by Z22 and FLAG-ZBP1 of the LINE 5' UTR region have positive values and identify features that are associated with Z-DNA formation in cells. **h**, MEFs treated with or without CBL0137 (5μM) for 12 hrs were stained for Z-DNA (red) and PML (green). **i**, Quantification of PML foci in CBL0137 untreated or treated cells. Data are mean ± s.d. (n = 30 in **c** or n = 5 in **i** per group). Two-tailed unpaired t-test with Welch's correction (**i**). ***$P < 0.0005$ ($P < 0.0001$ in **i**). Data are representative of at least three independent experiments.

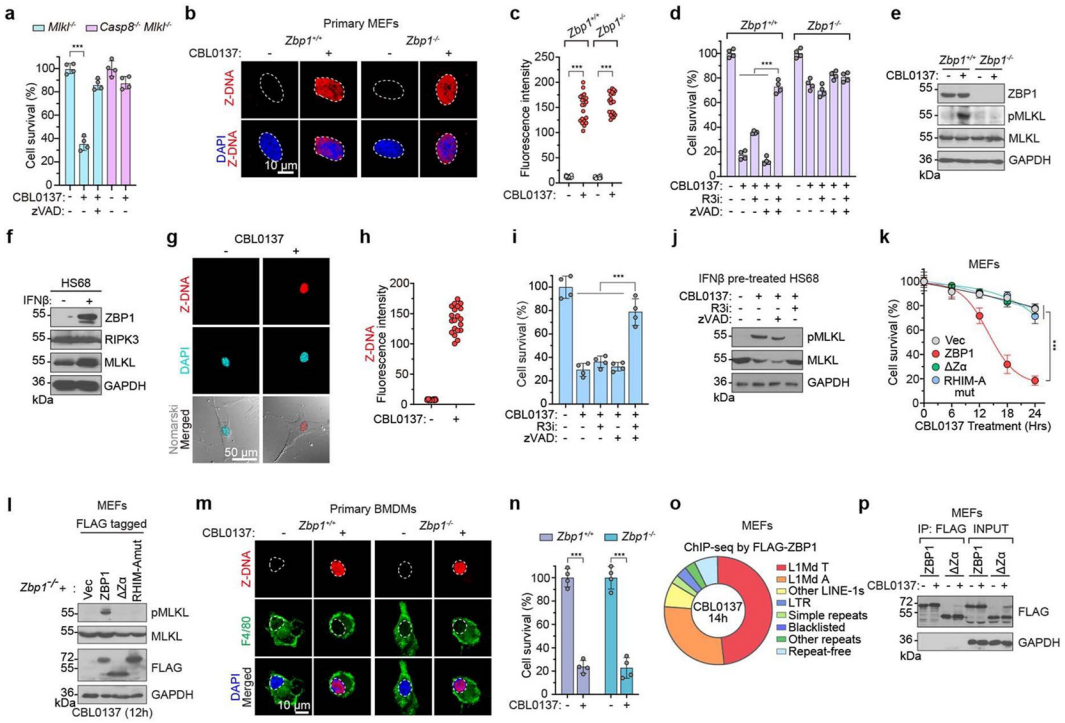

Extended Data Fig. 5. ZBP1-dependent cell death induced by CBL0137.

a, *Mlkl*$^{-/-}$ or *Mlkl*$^{-/-}$*Casp8*$^{-/-}$ MEFs were treated or untreated with CBL0137 (5 μM) in the presence or absence of zVAD (50 mM) and viability was examined at 18 hrs post treatment. **b**, Z-DNA formation in primary early-passage (p<5) *Zbp1*$^{+/+}$ and littermate control *Zbp1*$^{-/-}$ MEFs treated with CBL0137 (5 μM). **c**, Quantification of fluorescence intensity of Z-DNA signals in **b**. **d**, *Zbp1*$^{+/+}$ and *Zbp1*$^{-/-}$ MEFs were treated with CBL0137 (5 μM) in the presence or absence of zVAD (50 mM) and RIPK3 inhibitor (R3i) GSK'843 (5 μM) and viability was examined at 18 hrs post treatment. **e**, Immunoblot analysis of ZBP1-dependent MLKL activation in primary MEFs. **f**, Immunoblots showing levels of ZBP1, RIPK3 and MLKL in the human fibroblast cell line HS68 in the presence or absence of hIFNβ (100 ng/mL, 6 hrs). **g**, Z-DNA formation in HS68 cells treated with CBL0137 (5 μM, 12 hrs). **h**, Quantification of fluorescence intensity of Z-DNA signals in **g**. **i**, hIFNβ pretreated (100 ng/mL, 6 hrs) HS68 cells were exposed to CBL0137 in the presence or absence of zVAD (50 mM) and RIPK3 inhibitor (R3i, GSK'872, 5 μM) and viability was examined at 36 hrs post treatment. **j**, MLKL activation in hIFNβ pretreated (100 ng/mL, 6 hrs) HS68 cells treated with CBL0137 in the presence or absence of zVAD (50 mM) and RIPK3 inhibitor (R3i, GSK'872, 5 μM) was examined by immunoblot analysis 30 hrs post-CBL0137 treatment. **k**, CBL0137-induced cell death kinetics in *Zbp1*$^{-/-}$ MEFs stably reconstituted with empty vector (Vec), FLAG-ZBP1, or its mutants. **l**, Immunoblot analysis of MLKL activation in *Zbp1*$^{-/-}$ MEFs reconstituted with empty vector (Vec), FLAG-ZBP1, or FLAG-ZBP1 mutants after CBL0137 treatment. **m**, Primary *Zbp1*$^{+/+}$ and littermate-matched *Zbp1*$^{-/-}$ BMDMs were treated with CBL0137 (5 μM, 18 hrs) and stained for Z-DNA (red) and the macrophage marker F4/80 (green). **n**, Primary *Zbp1*$^{+/+}$ and *Zbp1*$^{-/-}$ BMDMs were treated with CBL0137 (5 μM) and viability was examined at 24 hrs post treatment. **o**, Distribution of FLAG-enriched peaks following treatment with CBL0137 (5μM) for 14 hrs.

p, Immortalized *Zbp1*$^{-/-}$ MEFs stably reconstituted with either FLAG-ZBP1 or FLAG- ΔZα mutant were treated with CBL0137 (1.5 μM, 14 hrs), and anti-FLAG immunoprecipitates were examined for FLAG. Whole-cell extract (5% input) was examined in parallel for FLAG. GAPDH was used as a loading control. Data are mean ± s.d. (n = 4 in **a**, **d**, **i**, **k**, **n** or n = 20 in **c**, **h** per group). Two-tailed unpaired t-test with Welch's correction (**a**, **c**, **n**), one-way ANOVA test (**d**, **i**) or two-way ANOVA test (**k**). ***P < 0.0005 (P = 0.0002 in **a**, P < 0.0001 in **c**, **d**, **i**, **k**, **n**). Data are representative of at least three independent experiments.

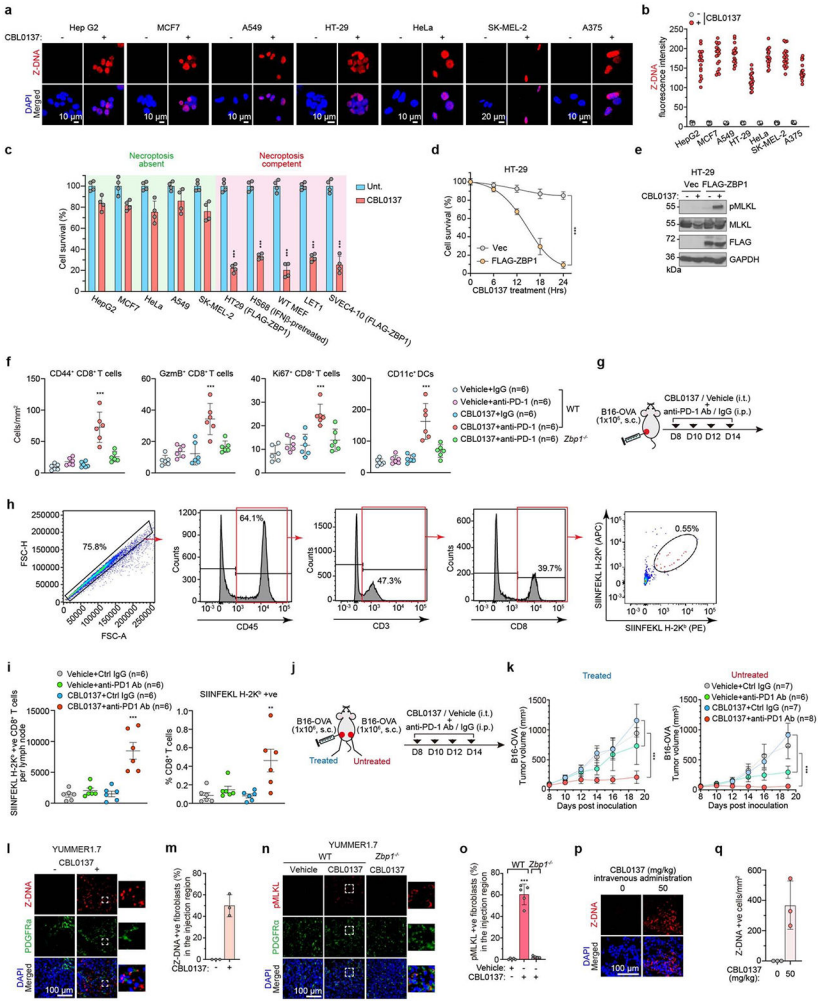

Extended Data Fig. 6. CBL0137 induced Z-DNA and immunogenicity.
a, HepG2, MCF7, A549, HT-29, HeLa, SK-MEL-2 or A375 human cell lines were treated with CBL0137 (5μM) for 12 hrs and stained for Z-DNA. **b**, Quantification of fluorescence intensity of Z-DNA signal in **a**. **c**, Cell lines deficient in necroptosis effector expression (HepG2, MCF7, A549, HeLa or SK-MEL-2) or those with intact/reconstituted necroptosis signaling (HT-29 cells reconstituted with FLAG-hZBP1, HS68 cells pretreated with hIFNβ (100 ng/mL) for 6 hrs, WT MEFs, LET1 murine airway epithelial cells, or SVEC4–10 murine endothelial cells stably reconstituted with FLAG-mZBP1) were treated with CBL0137 (5μM), and cell viability was examined 24 hrs (or 36 hrs for HS68 cells) after

CBL0137 treatment. **d**, CBL0137-induced cell death kinetics in HT-29 cells reconstituted with empty vector (Vec) or FLAG-hZBP1. **e**, Whole-cell extracts from human HT-29 cells stably expressing empty vector or FLAG-hZBP1 and treated with CBL0137 were examined for phosphorylated MLKL and FLAG-hZBP1 by immunoblot analysis. **f**, Mice bearing subcutaneous B16-F10 melanoma tumors were treated as shown in Figure 5h. Tumors were collected following four cycles of CBL0137 (20 μM, intratumoral injection) and anti-PD1 antibody (200 μg/mouse, i.p. injection). Frozen sections prepared from these tumors were co-stained for immunofluorescence detection of $CD8^+$ $CD44^+$, $CD8^+$ $GzmB^+$ or $CD8^+$ $Ki67^+$ T cells, or $CD11c^+$ DCs. **g**, Treatment schedule of mice bearing syngeneic subcutaneous B16-OVA melanoma syngeneic model. Treatments were initiated at 8 days post inoculation of tumor cells, on mice with similar tumor volumes (~100 mm^3). **h**, Gating strategy for identification of OVA-specific (SIINFEKL H-$2K^{b+}$) $CD8^+$ T cells. **i**, Total numbers of OVA-specific $CD8^+$ T cells isolated from tumor-draining inguinal lymph node (left panel) and frequencies of OVA-specific $CD8^+$ T cells in the tumor-draining inguinal lymph node, as a fraction of total $CD8^+$ T cells (right panel) are shown. **j**, Treatment schedule of mice bearing bilateral B16-OVA melanomas. Treatments were initiated at 8 days post inoculation of tumor cells, on mice with similar tumor volumes (~100 mm^3). **k**, Tumor growth curves of CBL0137-treated (ipsilateral) and untreated (contralateral) B16-OVA tumors following the indicated treatments. **l**, Immunofluorescence staining for fibroblasts (PDGFRα, green) and Z-DNA (red) in YUMMER1.7 melanoma sections from CBL0137 (intra-tumoral, 20 μM)-treated or untreated WT mice. M, Quantification of the proportion of Z-DNA positive fibroblasts in **l**. **n**, Vehicle or CBL0137 injected YUMMER1.7 tumors in WT or *Zbp1*$^{-/-}$ mice were stained for PDGFRα (green) or pMLKL (red). Nuclei are stained with DAPI (blue). **(o).** Quantification of $pMLKL^+$ fibroblasts in **n**. **p**, Immunofluorescence staining for Z-DNA (red) and DAPI (blue) in B16-F10 melanoma tumor sections from CBL0137 treated or untreated mice, 24 hrs after intravenous administration of drug at 50 mg/kg. **q**, Quantification of Z-DNA positive cells in **p**. Data are mean ± s.d. in **c**, **d**, **m**, **o**, **q** or s.e.m. in **f**, **i**, **k** (n = 20 in **b**, n = 4 in **c**, **d**, n = 6 in **f**, **i**, n = 3 in **m**, **q** or n = 5 in **o** per group). Two-tailed unpaired t-test with Welch's correction (**c**), one-way ANOVA test (**f**, **i**, **o**) or two-way ANOVA test (**d**, **k**). $^{**}P < 0.005$ ($P = 0.0015$ in **i**), $^{***}P < 0.0005$ ($P < 0.0001$ in **d**, **f**, **i**, **k**, **o**). Data are representative of at least three independent experiments.

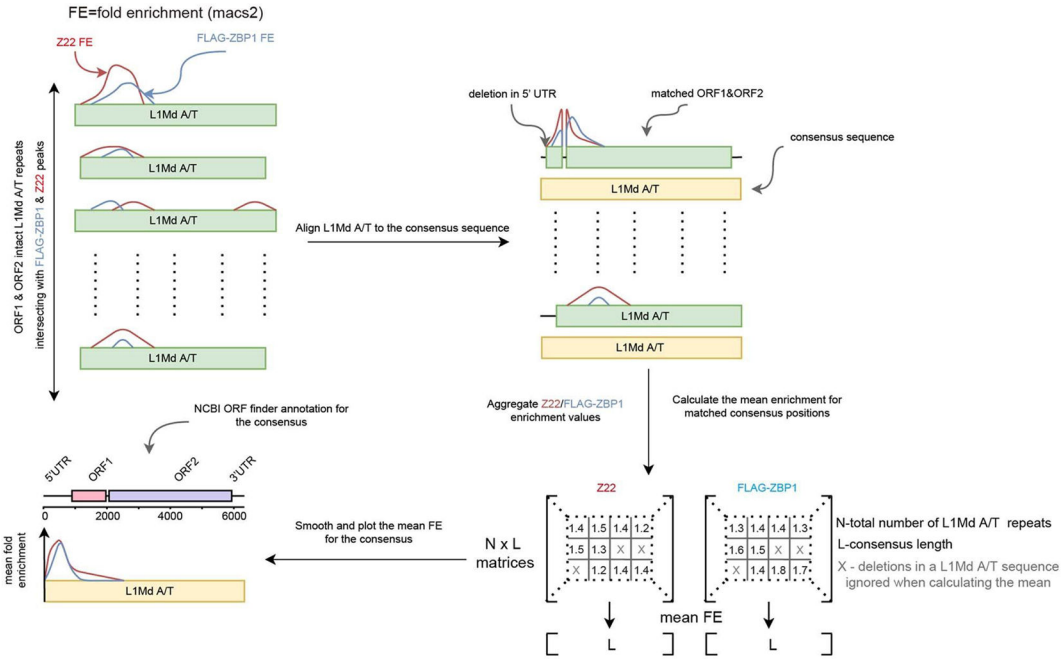

Extended Data Fig. 7. Flow chart showing the algorithm used to construct enrichment profiles for L1Md A and L1Md T repeats in Z22 and FLAG-ZBP1 ChIP-Seq datasets.

Following mapping to L1 elements, reads were normalized and aligned to consensus L1 sequences derived from the UCSC genome browser RepeatMasker tracks for the mouse assembly mm10. The enrichment values at each position were calculated and smoothed as described in Supplementary Methods and aligned with the NCBI annotation of LI open reading frames.

Supplementary Material

Refer to Web version on PubMed Central for supplementary material.

Acknowledgements.

We are grateful to Ekaterina Gurova for CBL0137 analogs. We thank Marcus Bosenberg, Jason Upton, Alexei Degterev, and Doug Green for providing cell lines or antibodies, Mark Andrake for help with molecular modeling, and Ankita Gupte and Zhen Liang for technical assistance. This work was supported by a gift from David Wiest and the Seeds of Hope foundation of the Bucks County Board of Associates to S.B, NIH grants CA168621, CA190542, AI135025, and AI144400 to S.B, and NIH grant GM119398 to V.S. CW was supported by National Health and Medical Research Council, Australia (NHMRC; APP1144049 and APP1183553). J.C.C. and P.G.T. were supported by the Mark Foundation, NIH grant U01AI150747, and the American Lebanese Syrian Associated Charities at St. Jude Children's Hospital. Additional funds were provided by NIH Cancer Center Support Grant P30CA006927 to SB. A.F., N.B., and M.P. are supported by the Basic Research Program of the National Research University Higher School of Economics, for which A. H. is an International Supervisor.

References.

1. Liu H et al. Tumor-derived IFN triggers chronic pathway agonism and sensitivity to ADAR loss. Nat Med 25, 95–102, doi:10.1038/s41591-018-0302-5 (2019). [PubMed: 30559422]
2. Ishizuka JJ et al. Loss of ADAR1 in tumours overcomes resistance to immune checkpoint blockade. Nature 565, 43–48, doi:10.1038/s41586-018-0768-9 (2019). [PubMed: 30559380]

3. Mehdipour P et al. Epigenetic therapy induces transcription of inverted SINEs and ADAR1 dependency. Nature 588, 169–173, doi:10.1038/s41586-020-2844-1 (2020). [PubMed: 33087935]
4. Gannon HS et al. Identification of ADAR1 adenosine deaminase dependency in a subset of cancer cells. Nat Commun 9, 5450, doi:10.1038/s41467-018-07824-4 (2018). [PubMed: 30575730]
5. Chen R, Ishak CA & De Carvalho DD Endogenous Retroelements and the Viral Mimicry Response in Cancer Therapy and Cellular Homeostasis. Cancer Discov 11, 2707–2725, doi:10.1158/2159-8290.CD-21-0506 (2021). [PubMed: 34649957]
6. Loo Yau H, Ettayebi I & De Carvalho DD The Cancer Epigenome: Exploiting Its Vulnerabilities for Immunotherapy. Trends Cell Biol 29, 31–43, doi:10.1016/j.tcb.2018.07.006 (2019). [PubMed: 30153961]
7. Heraud-Farlow JE, Chalk AM & Walkley CR Defining the functions of adenosine-to-inosine RNA editing through hematology. Curr Opin Hematol 26, 241–248, doi:10.1097/MOH.0000000000000514 (2019). [PubMed: 31033705]
8. Eisenberg E & Levanon EY A-to-I RNA editing - immune protector and transcriptome diversifier. Nat Rev Genet 19, 473–490, doi:10.1038/s41576-018-0006-1 (2018). [PubMed: 29692414]
9. Samuel CE Adenosine deaminase acting on RNA (ADAR1), a suppressor of double-stranded RNA-triggered innate immune responses. J Biol Chem 294, 1710–1720, doi:10.1074/jbc.TM118.004166 (2019). [PubMed: 30710018]
10. Herbert A ALU non-B-DNA conformations, flipons, binary codes and evolution. R Soc Open Sci 7, 200222, doi:10.1098/rsos.200222 (2020). [PubMed: 32742689]
11. Chung H et al. Human ADAR1 Prevents Endogenous RNA from Triggering Translational Shutdown. Cell 172, 811–824 e814, doi:10.1016/j.cell.2017.12.038 (2018). [PubMed: 29395325]
12. George CX, Ramaswami G, Li JB & Samuel CE Editing of Cellular Self-RNAs by Adenosine Deaminase ADAR1 Suppresses Innate Immune Stress Responses. J Biol Chem 291, 6158–6168, doi:10.1074/jbc.M115.709014 (2016). [PubMed: 26817845]
13. Liddicoat BJ et al. RNA editing by ADAR1 prevents MDA5 sensing of endogenous dsRNA as nonself. Science 349, 1115–1120, doi:10.1126/science.aac7049 (2015). [PubMed: 26275108]
14. Herbert A et al. A Z-DNA binding domain present in the human editing enzyme, double-stranded RNA adenosine deaminase. Proc Natl Acad Sci U S A 94, 8421–8426 (1997). [PubMed: 9237992]
15. Herbert A Mendelian disease caused by variants affecting recognition of Z-DNA and Z-RNA by the Zalpha domain of the double-stranded RNA editing enzyme ADAR. Eur J Hum Genet 28, 114–117, doi:10.1038/s41431-019-0458-6 (2020). [PubMed: 31320745]
16. Zhang T et al. Influenza Virus Z-RNAs Induce ZBP1-Mediated Necroptosis. Cell 180, 1115–1129 e1113, doi:10.1016/j.cell.2020.02.050 (2020). [PubMed: 32200799]
17. Hardin CC et al. Stabilization of Z-RNA by chemical bromination and its recognition by anti-Z-DNA antibodies. Biochemistry 26, 5191–5199 (1987). [PubMed: 2444254]
18. Schade M, Turner CJ, Lowenhaupt K, Rich A & Herbert A Structure-function analysis of the Z-DNA-binding domain Zalpha of dsRNA adenosine deaminase type I reveals similarity to the (alpha + beta) family of helix-turn-helix proteins. EMBO J 18, 470–479, doi:10.1093/emboj/18.2.470 (1999). [PubMed: 9889202]
19. Bazak L, Levanon EY & Eisenberg E Genome-wide analysis of Alu editability. Nucleic Acids Res 42, 6876–6884, doi:10.1093/nar/gku414 (2014). [PubMed: 24829451]
20. Nichols PJ et al. Recognition of non-CpG repeats in Alu and ribosomal RNAs by the Z-RNA binding domain of ADAR1 induces A-Z junctions. Nature Communications 12, 793, doi:10.1038/s41467-021-21039-0 (2021).
21. Balasubramaniyam T, Ishizuka T, Xiao CD, Bao HL & Xu Y 2'-O-Methyl-8-methylguanosine as a Z-Form RNA Stabilizer for Structural and Functional Study of Z-RNA. Molecules 23, 2572–2579, doi:10.3390/molecules23102572 (2018).
22. Brown BA 2nd, Lowenhaupt K, Wilbert CM, Hanlon EB & Rich A The zalpha domain of the editing enzyme dsRNA adenosine deaminase binds left-handed Z-RNA as well as Z-DNA. Proc Natl Acad Sci U S A 97, 13532–13536, doi:10.1073/pnas.240464097 (2000). [PubMed: 11087828]

23. Kim K et al. Solution structure of the Zbeta domain of human DNA-dependent activator of IFN-regulatory factors and its binding modes to B- and Z-DNAs. Proc Natl Acad Sci U S A 108, 6921–6926, doi:10.1073/pnas.1014898107 (2011). [PubMed: 21471454]

24. Peck LJ, Nordheim A, Rich A & Wang JC Flipping of cloned d(pCpG)n.d(pCpG)n DNA sequences from right- to left-handed helical structure by salt, Co(III), or negative supercoiling. Proc Natl Acad Sci U S A 79, 4560–4564, doi:10.1073/pnas.79.15.4560 (1982). [PubMed: 6956879]

25. Chang HW et al. Histone Chaperone FACT and Curaxins: Effects on Genome Structure and Function. J Cancer Metastasis Treat 5, doi:10.20517/2394-4722.2019.31 (2019).

26. Safina A et al. FACT is a sensor of DNA torsional stress in eukaryotic cells. Nucleic Acids Res 45, 1925–1945, doi:10.1093/nar/gkw1366 (2017). [PubMed: 28082391]

27. Sookdeo A, Hepp CM, McClure MA & Boissinot S Revisiting the evolution of mouse LINE-1 in the genomic era. Mob DNA 4, 3, doi:10.1186/1759-8753-4-3 (2013). [PubMed: 23286374]

28. Beknazarov N, Jin S & Poptsova M Deep learning approach for predicting functional Z-DNA regions using omics data. Sci Rep 10, 19134, doi:10.1038/s41598-020-76203-1 (2020). [PubMed: 33154517]

29. Bao HL & Xu Y Observation of Z-DNA Structure via the Synthesis of Oligonucleotide DNA Containing 8-Trifluoromethyl-2-Deoxyguanosine. Curr Protoc 1, e28, doi:10.1002/cpz1.28 (2021). [PubMed: 33484490]

30. Jeronimo C, Watanabe S, Kaplan CD, Peterson CL & Robert F The Histone Chaperones FACT and Spt6 Restrict H2A.Z from Intragenic Locations. Mol Cell 58, 1113–1123, doi:10.1016/j.molcel.2015.03.030 (2015). [PubMed: 25959393]

31. Denli AM et al. Primate-specific ORF0 contributes to retrotransposon-mediated diversity. Cell 163, 583–593, doi:10.1016/j.cell.2015.09.025 (2015). [PubMed: 26496605]

32. Somers K et al. Potent antileukemic activity of curaxin CBL0137 against MLL-rearranged leukemia. Int J Cancer 146, 1902–1916, doi:10.1002/ijc.32582 (2020). [PubMed: 31325323]

33. Gasparian AV et al. Curaxins: anticancer compounds that simultaneously suppress NF-kappaB and activate p53 by targeting FACT. Sci Transl Med 3, 95ra74, doi:10.1126/scitranslmed.3002530 (2011).

34. Carter DR et al. Therapeutic targeting of the MYC signal by inhibition of histone chaperone FACT in neuroblastoma. Sci Transl Med 7, 312ra176, doi:10.1126/scitranslmed.aab1803 (2015).

35. Koo GB et al. Methylation-dependent loss of RIP3 expression in cancer represses programmed necrosis in response to chemotherapeutics. Cell Res 25, 707–725, doi:10.1038/cr.2015.56 (2015). [PubMed: 25952668]

36. Gabrilovich DI & Nagaraj S Myeloid-derived suppressor cells as regulators of the immune system. Nat Rev Immunol 9, 162–174, doi:10.1038/nri2506 (2009). [PubMed: 19197294]

37. Weiss SA, Wolchok JD & Sznol M Immunotherapy of Melanoma: Facts and Hopes. Clin Cancer Res 25, 5191–5201, doi:10.1158/1078-0432.CCR-18-1550 (2019). [PubMed: 30923036]

38. Wang J et al. UV-induced somatic mutations elicit a functional T cell response in the YUMMER1.7 mouse melanoma model. Pigment Cell Melanoma Res 30, 428–435, doi:10.1111/pcmr.12591 (2017). [PubMed: 28379630]

39. Nirschl CJ et al. IFNgamma-Dependent Tissue-Immune Homeostasis Is Co-opted in the Tumor Microenvironment. Cell 170, 127–141 e115, doi:10.1016/j.cell.2017.06.016 (2017). [PubMed: 28666115]

40. Benci JL et al. Tumor Interferon Signaling Regulates a Multigenic Resistance Program to Immune Checkpoint Blockade. Cell 167, 1540–1554 e1512, doi:10.1016/j.cell.2016.11.022 (2016). [PubMed: 27912061]

References.

1. Ishii KJ et al. TANK-binding kinase-1 delineates innate and adaptive immune responses to DNA vaccines. Nature 451, 725–729, doi:nature06537 [pii] 10.1038/nature06537 (2008). [PubMed: 18256672]

2. Liddicoat BJ et al. RNA editing by ADAR1 prevents MDA5 sensing of endogenous dsRNA as nonself. Science 349, 1115–1120, doi:10.1126/science.aac7049 (2015). [PubMed: 26275108]
3. Bao HL & Xu Y Observation of Z-DNA Structure via the Synthesis of Oligonucleotide DNA Containing 8-Trifluoromethyl-2-Deoxyguanosine. Curr Protoc 1, e28, doi:10.1002/cpz1.28 (2021). [PubMed: 33484490]
4. Chen P et al. Anti-CD70 Immunocytokines for Exploitation of Interferon-gamma-Induced RIP1-Dependent Necrosis in Renal Cell Carcinoma. PLoS One 8, e61446, doi:10.1371/journal.pone.0061446 PONE-D-13-01743[pii] (2013). [PubMed: 23613854]
5. Cancer Genome Atlas N Genomic Classification of Cutaneous Melanoma. Cell 161, 1681–1696, doi:10.1016/j.cell.2015.05.044 (2015). [PubMed: 26091043]
6. Becht E et al. Estimating the population abundance of tissue-infiltrating immune and stromal cell populations using gene expression. Genome Biol 17, 218, doi:10.1186/s13059-016-1070-5 (2016). [PubMed: 27765066]
7. Ishizuka JJ et al. Loss of ADAR1 in tumours overcomes resistance to immune checkpoint blockade. Nature 565, 43–48, doi:10.1038/s41586-018-0768-9 (2019). [PubMed: 30559380]
8. Gabitova-Cornell L et al. Cholesterol Pathway Inhibition Induces TGF-beta Signaling to Promote Basal Differentiation in Pancreatic Cancer. Cancer Cell 38, 567–583 e511, doi:10.1016/j.ccell.2020.08.015 (2020). [PubMed: 32976774]
9. Satija R, Farrell JA, Gennert D, Schier AF & Regev A Spatial reconstruction of single-cell gene expression data. Nat Biotechnol 33, 495–502, doi:10.1038/nbt.3192 (2015). [PubMed: 25867923]
10. Patro R, Duggal G, Love MI, Irizarry RA & Kingsford C Salmon provides fast and bias-aware quantification of transcript expression. Nat Methods 14, 417–419, doi:10.1038/nmeth.4197 (2017). [PubMed: 28263959]
11. Love MI, Huber W & Anders S Moderated estimation of fold change and dispersion for RNA-seq data with DESeq2. Genome Biol 15, 550, doi:10.1186/s13059-014-0550-8 (2014). [PubMed: 25516281]
12. Bachu M et al. A versatile mouse model of epitope-tagged histone H3.3 to study epigenome dynamics. J Biol Chem 294, 1904–1914, doi:10.1074/jbc.RA118.005550 (2019). [PubMed: 30552116]
13. Roth SH, Levanon EY & Eisenberg E Genome-wide quantification of ADAR adenosine-to-inosine RNA editing activity. Nat Methods 16, 1131–1138, doi:10.1038/s41592-019-0610-9 (2019). [PubMed: 31636457]
14. Gruber AR, Lorenz R, Bernhart SH, Neubock R & Hofacker IL The Vienna RNA websuite. Nucleic Acids Res 36, W70–74, doi:10.1093/nar/gkn188 (2008). [PubMed: 18424795]
15. Lo Giudice C, Tangaro MA, Pesole G & Picardi E Investigating RNA editing in deep transcriptome datasets with REDItools and REDIportal. Nat Protoc 15, 1098–1131, doi:10.1038/s41596-019-0279-7 (2020). [PubMed: 31996844]
16. Anders S, Pyl PT & Huber W HTSeq--a Python framework to work with high-throughput sequencing data. Bioinformatics 31, 166–169, doi:10.1093/bioinformatics/btu638 (2015). [PubMed: 25260700]
17. Kechin A, Boyarskikh U, Kel A & Filipenko M cutPrimers: A New Tool for Accurate Cutting of Primers from Reads of Targeted Next Generation Sequencing. J Comput Biol 24, 1138–1143, doi:10.1089/cmb.2017.0096 (2017). [PubMed: 28715235]
18. Li H Minimap2: pairwise alignment for nucleotide sequences. Bioinformatics 34, 3094–3100, doi:10.1093/bioinformatics/bty191 (2018). [PubMed: 29750242]
19. Li H et al. The Sequence Alignment/Map format and SAMtools. Bioinformatics 25, 2078–2079, doi:10.1093/bioinformatics/btp352 (2009). [PubMed: 19505943]
20. Zhang Y et al. Model-based analysis of ChIP-Seq (MACS). Genome Biol 9, R137, doi:10.1186/gb-2008-9-9-r137 (2008). [PubMed: 18798982]
21. Zhu LJ et al. ChIPpeakAnno: a Bioconductor package to annotate ChIP-seq and ChIP-chip data. BMC Bioinformatics 11, 237, doi:10.1186/1471-2105-11-237 (2010). [PubMed: 20459804]
22. Gu Z, Gu L, Eils R, Schlesner M & Brors B circlize Implements and enhances circular visualization in R. Bioinformatics 30, 2811–2812, doi:10.1093/bioinformatics/btu393 (2014). [PubMed: 24930139]

23. Penzkofer T et al. L1Base 2: more retrotransposition-active LINE-1s, more mammalian genomes. Nucleic Acids Res 45, D68–D73, doi:10.1093/nar/gkw925 (2017). [PubMed: 27924012]

24. Sievers F et al. Fast, scalable generation of high-quality protein multiple sequence alignments using Clustal Omega. Mol Syst Biol 7, 539, doi:10.1038/msb.2011.75 (2011). [PubMed: 21988835]

25. Ho PS, Ellison MJ, Quigley GJ & Rich A A computer aided thermodynamic approach for predicting the formation of Z-DNA in naturally occurring sequences. EMBO J 5, 2737–2744 (1986). [PubMed: 3780676]

26. Denli AM et al. Primate-specific ORF0 contributes to retrotransposon-mediated diversity. Cell 163, 583–593, doi:10.1016/j.cell.2015.09.025 (2015). [PubMed: 26496605]

27. Oki S et al. ChIP-Atlas: a data-mining suite powered by full integration of public ChIP-seq data. EMBO Rep 19, doi:10.15252/embr.201846255 (2018).

28. Beknazarov N, Jin S & Poptsova M Deep learning approach for predicting functional Z-DNA regions using omics data. Sci Rep 10, 19134, doi:10.1038/s41598-020-76203-1 (2020). [PubMed: 33154517]

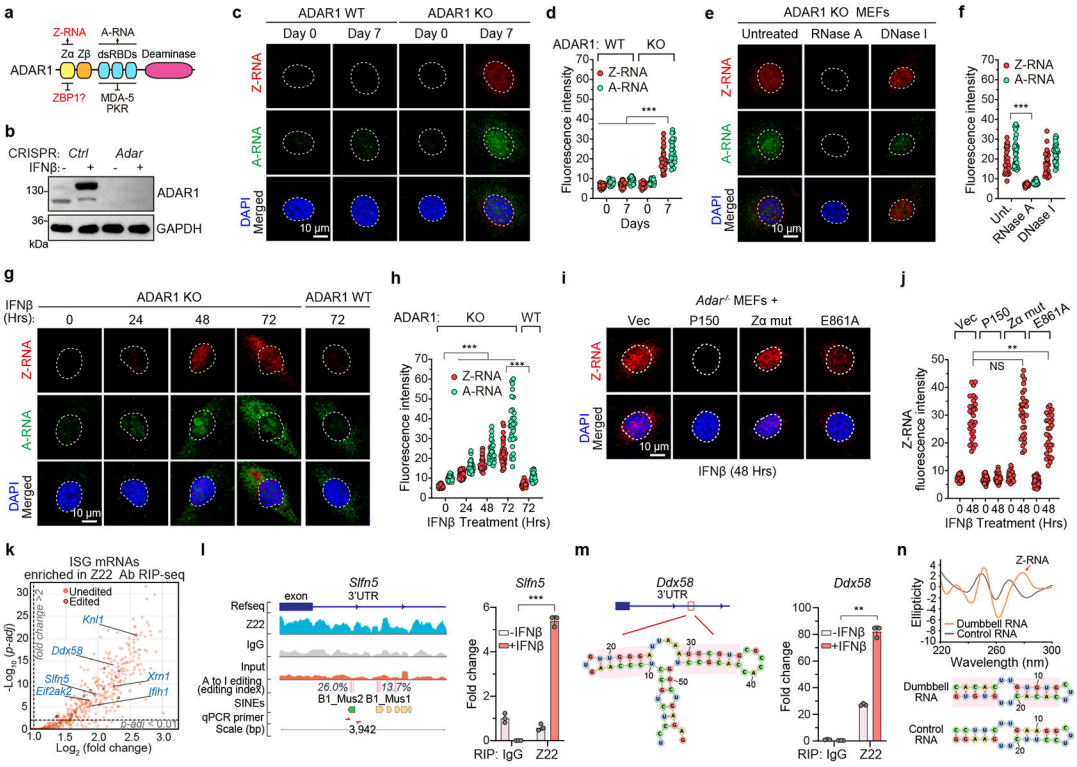

Figure 1. ADAR1 suppresses endogenous Z-RNAs.

a, Schematic of ADAR1 structure. **b**, Levels of ADAR1 p150 and p110 isoforms in MEFs± IFNβ (100 ng/mL, 24 hrs) after transfection with recombinant Cas9 protein and either luciferase (ADAR1 WT) or murine *Adar* (ADAR1 KO) sgRNA. (**c**, **e**, **g**), Z-RNA and A-RNA accumulation in ADAR1 WT or ADAR1 KO cells, (**d**, **f**, **h**), Fluorescence intensity of Z-RNA and A-RNA signals in **c**, **e**, **g**. **i**, Z-RNA accumulation in immortalized *Adar*$^{-/-}$ MEFs stably reconstituted with empty vector (Vec), ADAR1 p150, Zα N175A/Y179A (Zα mut), or editing-deficient (E861A) mutants, ± IFNβ (100 ng/mL). **j**, Fluorescence intensity of Z-RNA signal in **i** and Extended Data Fig. 1p. **k**, ISG mRNAs enriched in Z22 Ab RIP-Seq from immortalized ADAR1 KO *Zbp1*$^{-/-}$ MEFs ± IFNβ (100 ng/mL, 48 hrs). **l**, *Slfn5* mRNA 3'UTR showing Z22 enrichment (blue peaks), IgG (grey peaks), input (orange peaks), editing sites (vertical red bars), SINE and qPCR primers (red arrows) location. qPCR of *Slfn5* mRNA 3'UTR following Z22 or control IgG IP from ADAR1 MEFs ± IFNβ (100 ng/mL, 48 hrs). **m**, qPCR of *Ddx58* mRNA 3'UTR (IP with Z22 or control IgG antibodies from ADAR1 KO MEFs). Potential bipartite (dumbbell) RNA structures (RNA-fold) with putative Zα binding sites outlined in pink boxes. **n**, CD spectra of synthetic dumbbell RNA structures and control RNA at 3M NaCl. Pink boxes encase putative Zα binding sites. Data are mean ± s.d. (n = 30 in **d**, **f**, **h**, **j** or n = 3 in **l**, **m** per group). One-way ANOVA test (**d**, **h**) or two-tailed unpaired t-test with Welch's correction (**f**, **h**, **j**, **l**, **m**). $^{**}P < 0.005$ ($P = 0.001$ in **m**, $P = 0.002$ in **j**), $^{***}P < 0.0005$ ($P < 0.0001$ in **d**, **f**, **h**); NS, no significance. Data are from at least three independent experiments.

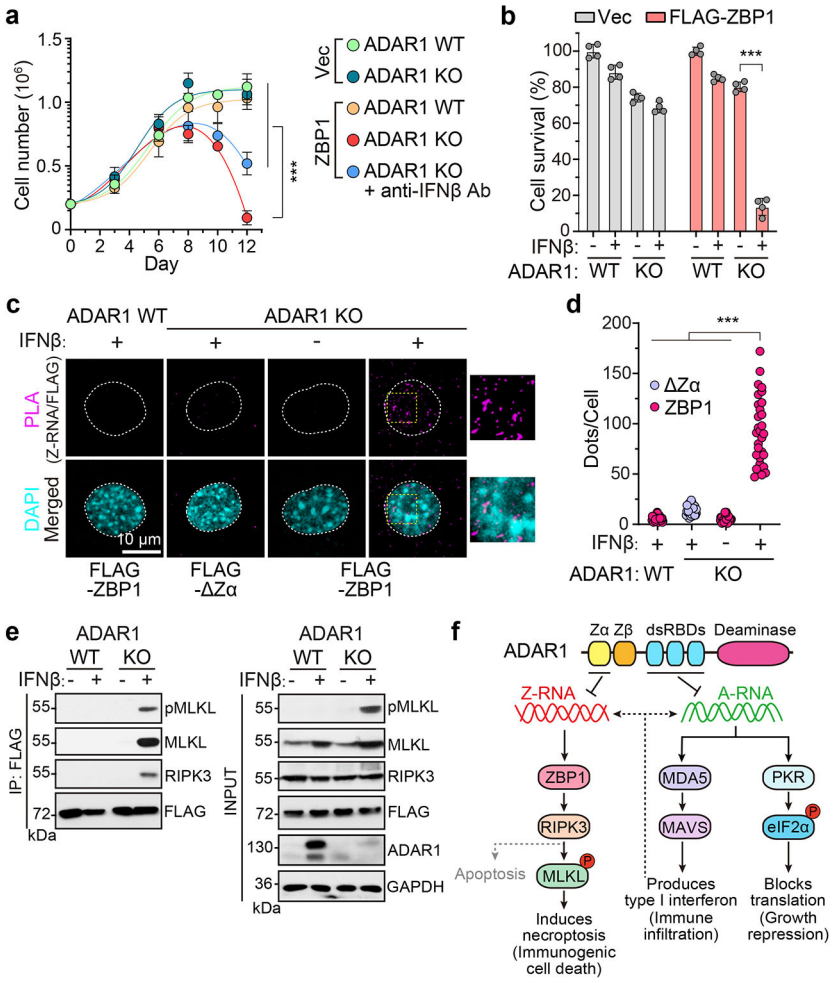

Figure 2. ADAR1 loss triggers ZBP1-dependent cell death.

a, Immortalized *Zbp1*$^{-/-}$ MEFs stably reconstituted with either an empty vector control (Vec) or FLAG-ZBP1 (ZBP1) were subjected to CRISPR-based control (ADAR1 WT) or ADAR1 ablation (ADAR1 KO) and their growth in the presence or absence of neutralizing anti-IFNβ antibodies (0.5 μg/mL) was monitored over 12 days. **b**, Viability of ADAR WT and ADAR KO 48 hrs post IFNβ (100 ng/mL) treatment. **c**, Proximity ligation assay (PLA) showing interaction between ZBP1 (but not the ZBP1 ΔZα mutant) and Z-RNA in IFNβ-treated cells when ADAR1 is ablated. Nuclei are stained with DAPI (cyan) and outlined with dashed white lines. Selected areas are shown magnified to the right of each image. **d**, Quantification of PLA-positive foci (purple dots) per cell in **c**. **e**, *Zbp1*$^{-/-}$ MEFs stably expressing FLAG-ZBP1 and either expressing (WT) or ablated for (KO) *Adar* were exposed to IFNβ (100 ng/mL, 48 hrs) and anti-FLAG immunoprecipitates from these cells were examined for RIPK3, MLKL and FLAG. Whole-cell extract (5% input) was examined in parallel for RIPK3, MLKL, FLAG-ZBP1 and ADAR1 proteins. **f**, ADAR1 suppresses both endogenous A-RNAs and Z-RNAs, preventing activation of MDA-5 and PKR responses downstream of A-RNA, and ZBP1-driven cell death downstream of Z-RNA. Data are mean ± s.d. (n = 4 in **a**, **b** or n = 30 in **d** per group). Two-way ANOVA test (**a**), two-tailed unpaired

t-test with Welch's correction (**b**) or one-way ANOVA test (**d**). ***$P < 0.0005$ ($P < 0.0001$ in **a**, **b**, **d**). Data are representative of at least three independent experiments.

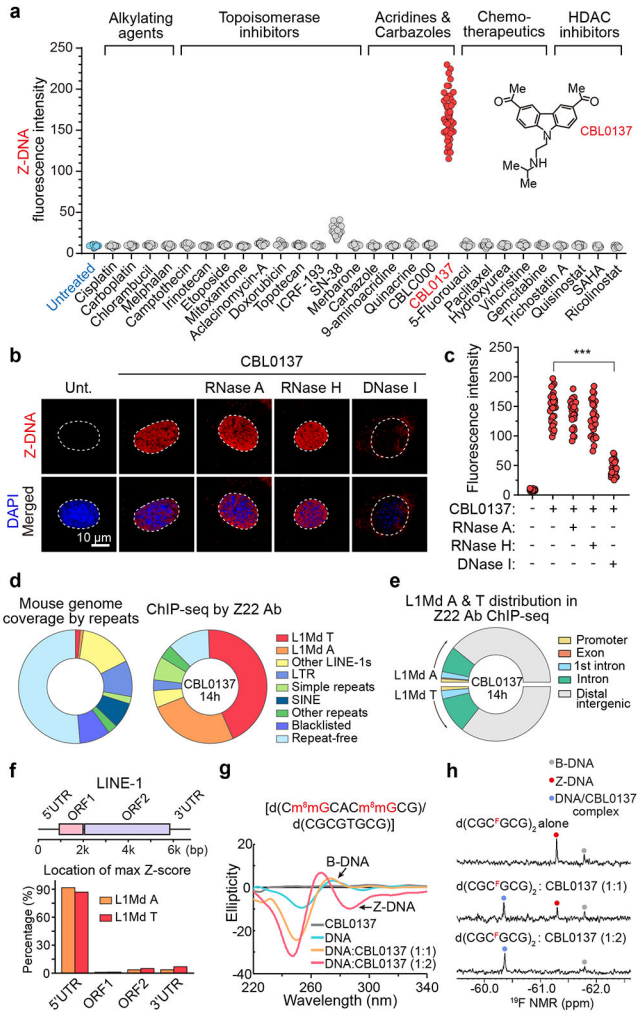

Figure 3. CBL0137 induces Z-DNA formation in cells.

a, Fluorescence intensity of Z-DNA signal after treatment of MEFs with equimolar (5μM) amounts of the indicated compounds for 18 hrs. **b**, WT MEFs fixed at 12 hrs post treatment with CBL0137 (5 μM) were exposed to the indicated nucleases for 45 min, before staining for Z-DNA. **c**, Quantification of fluorescence intensity of Z-DNA signal in **b**. **d**, Proportion of EREs and other repeats in the mouse genome (left), compared to distribution of Z22-enriched peaks following treatment with CBL0137 (1.5 μM) (right). **e**, Genomic distribution of L1Md T and L1Md A elements in Z22 pulldowns. **f**, Location of maximum Z-scores for L1Md T and L1Md A bound by Z22 in **e**. **g**, CD spectra of Z-prone B-DNA hexamer [d(Cm^{8}mGCACGCG)/d(CGCGTGCG)] in the presence or absence of CBL0137. **h**, ^{19}F NMR spectra of 8-trifluoromethyl-2′-deoxyguanosine Z-DNA d(CGC^{F}GCG)$_2$ in the presence of different ratios of CBL0137DNA. n = 30 per group in **a**, **c**. Two-tailed unpaired t-test with Welch's correction (**c**). ***$P < 0.0005$ ($P < 0.0001$ in **c**). Data are representative of at least three independent experiments.

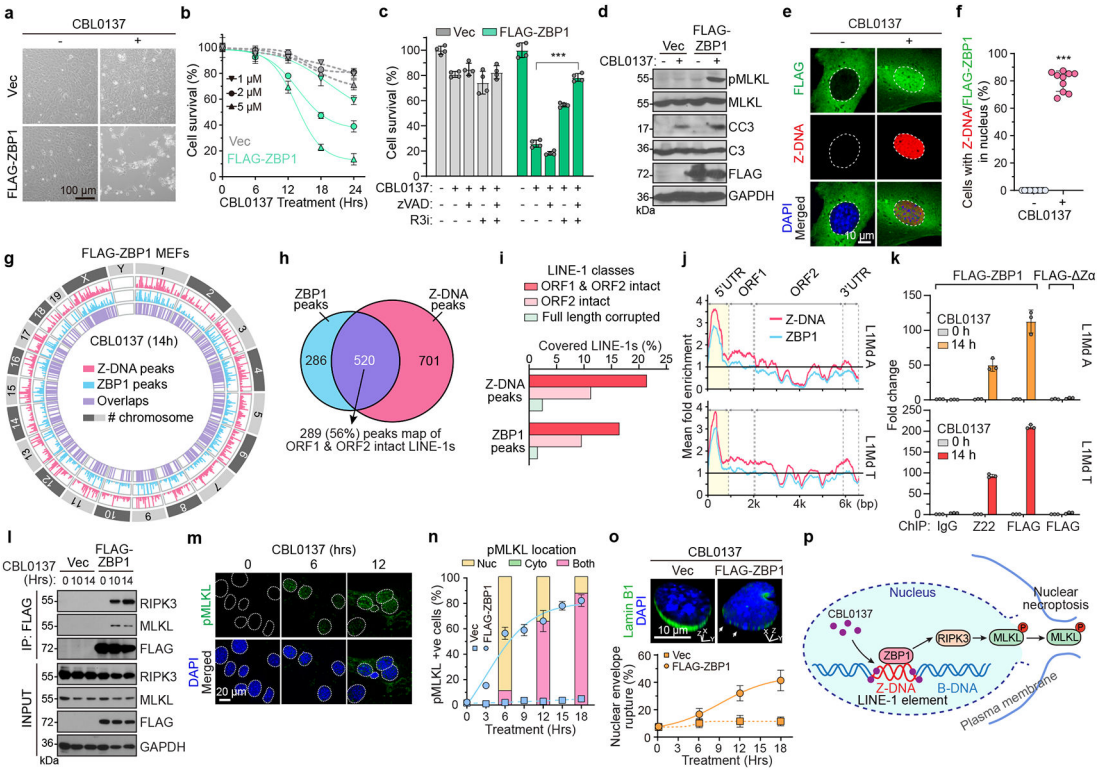

Figure 4. CBL0137 induces ZBP1-dependent cell death.

a, Photomicrographs of *Zbp1*$^{-/-}$ MEFs stably expressing empty vector (Vec) or FLAG-ZBP1 ± CBL0137 (5 μM) for 18 hrs. **b**, Kinetics of CBL0137-induced death in Vec and FLAG-ZBP1 MEFs. **(c).** Viability at 18 hrs of vec and FLAG-ZBP1 MEFs ± CBL0137 (5 μM), zVAD (50 mM) and RIPK3 inhibitor (R3i) GSK'843 (5 μM). **d**, Immunoblots of MLKL and caspase 3 activation. **e**, Immunofluorescence staining of FLAG-ZBP1 and Z-DNA in FLAG-ZBP1 MEFs treated with CBL0137 (5 μM) for 12 hrs. **f**, Quantitation of nuclear co-localized ZBP1 and Z-DNA in **e**. (**g**, **h**), Overlap and quantitation of Z22 and FLAG-ZBP1 genomic Z-DNA peaks after treatment with CBL0137. (**i**, **j**), L1 repeats, especially ORF1- and ORF2-intact L1Md A and L1Md T classes, are enriched in FLAG-ZBP1 and Z22 peaks from **g**. **k**, DNA eluted from antibody pulldowns of either FLAG-ZBP1 or FLAG-ZBP1 ΔZα mutant from stably transfected CBL0137-treated *Zbp1*$^{-/-}$ MEFs was examined by RT-qPCR for L1Md A and L1Md T. Data were normalized to Input. **l**, Vec and FLAG-ZBP1 MEFs were treated with CBL0137 (5 μM). Whole-cell extract (5% input) and anti-FLAG immunoprecipitates were examined for RIPK3, MLKL and FLAG in parallel. **m**, Immunofluorescence staining for pMLKL in FLAG-ZBP1 MEFs treated with CBL0137 (5 μM). (nuclei: dashed white lines). **n**, Kinetics of pMLKL positivity (Line graph,) and localization of pMLKL signal (bar graphs). **o**, 3D reconstruction (upper panels) of DNA herniating (arrows) through the nuclear envelope (stained with LaminB1) in CBL0137-treated MEFs over time (bottom panel). **p**, Proposed model for CBL0137-mediated nuclear necroptosis. Data are mean ± s.d. (n = 4 in **b**, **c**, **n**, **o**, n = 10 in **f** or n = 3 in **k** per group). Two-tailed unpaired t-test with Welch's correction (**c, f**). ***$P < 0.0005$ ($P < 0.0001$ in **c**, **f**). Data are from at least three independent experiments.

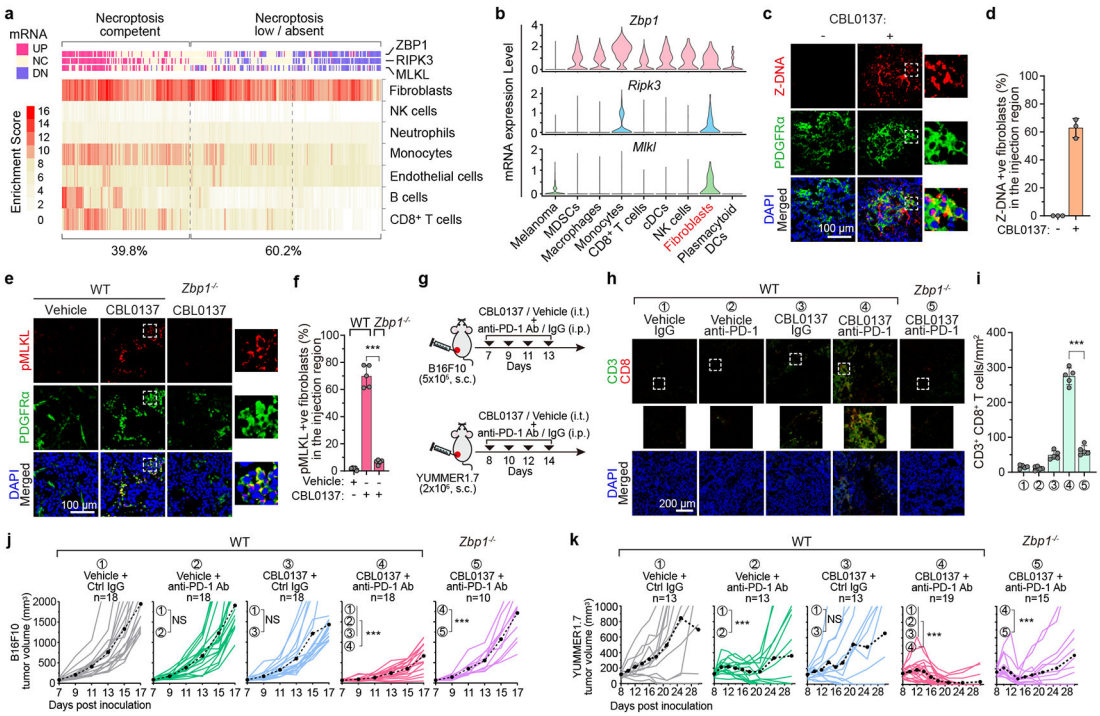

Figure 5. CBL0137 potentiates ICB responses in melanoma.

a, Enrichment scores of immune and stromal cell populations in cutaneous melanoma cases (TCGA). Upper panel shows heatmap of the $\log_2$ normalized gene expression values for *Zbp1, Ripk3* and *Mlkl*. **b**, Violin plots of the *Zbp1, Ripk3* and *Mlkl* expression distribution of different cell clusters from scRNA-seq data in Ishikuza *et al.*[2] **c**, Immunofluorescence staining for fibroblasts (PDGFRα) and Z-DNA in B16-F10 melanoma sections from CBL0137 (20 μM, intra-tumorally)-treated or untreated WT mice. **d**, Quantification of the proportion of Z-DNA positive fibroblasts in **c**. **e**, Vehicle or CBL0137 injected tumors in WT or *Zbp1*$^{-/-}$ mice were stained for PDGFRα or pMLKL. **f**, Quantification of fibroblasts with pMLKL in **e**. **g**, Treatment schedule of mice bearing subcutaneous B16-F10 or YUMMER1.7 melanomas. **h**, Immunofluorescence staining for CD8$^+$ and CD3$^+$ T cells in B16-F10 melanoma sections from WT or *Zbp1*$^{-/-}$ mice with the indicated treatments. **i**, Quantitation of CD8$^+$ T cells in **h**. (**j**, **k**), Individual tumor growth curves of B16-F10 (**j**) or YUMMER1.7 (**k**) tumor-bearing WT or *Zbp1*$^{-/-}$ mice following the indicated treatments. Data are mean ± s.d. (n = 3 in **d** or n = 5 in **f**, **i** per group). Two-tailed unpaired t-test with Welch's correction (**f**, **i**) or two-way ANOVA test (**j**, **k**). ***$P < 0.0005$ ($P < 0.0001$ in **f**, **i**, **j**, **k**); NS, no significance. Data are representative of at least three independent experiments.